Khalaj, Maryam; Zarabi Golkhatmi, Sanaz; Alem, Sayed Ali Ahmad; Baghchesaraee, Kahila; Hasanzadeh Azar, Mahdi; Angizi, Shayan

Recent Progress in the Study of Thermal Properties and Tribological Behaviors of Hexagonal Boron Nitride-Reinforced Composites

Published in:
Journal of Composites Science

DOI:
10.3390/jcs4030116

Published: 01/09/2020

Document Version
Publisher's PDF, also known as Version of record

Journal of
Composites Science

MDPI

Review

Recent Progress in the Study of Thermal Properties and Tribological Behaviors of Hexagonal Boron Nitride-Reinforced Composites

Maryam Khalaj [1], Sanaz Zarabi Golkhatmi [2], Sayed Ali Ahmad Alem [3], Kahila Baghchesaraee [4], Mahdi Hasanzadeh Azar [5] and Shayan Angizi [6,*]

1 Department of Materials Science and Engineering, Faculty of Engineering, Imam Khomeini International University, Qazvin 34149-16818, Iran; Maryam.khalaj@edu.ikiu.ac.ir
2 New Energy Technologies Group, Department of Applied Physics, Aalto University School of Science, P.O. Box 15100, FI-00076 Aalto, Finland; Sanaz.zarabigolkhatmi@aalto.fi
3 Department of Chemistry, Materials and Chemical Engineering, Politecnico di Milano, Piazza Leonardo da Vinci 32, 20133 Milan, Italy; Sayedali.alem@mail.polimi.it
4 Department of Materials Science and Engineering, Faculty of Materials and Metallurgical Engineering, University of Semnan, Semnan 35131-19111, Iran; Kahila.ba@outlook.com
5 Department of Materials Science and Engineering, Sharif University of Technology, Tehran 15119-43943, Iran; Mahdi.hassanzadeh@student.sharif.ir
6 Department of Chemistry and Chemical Biology, McMaster University, 1280 Main St. W., Hamilton, ON L8S 4L8, Canada
* Correspondence: angizis@mcmaster.ca

Received: 20 July 2020; Accepted: 6 August 2020; Published: 14 August 2020

Abstract: Ever-increasing significance of composite materials with high thermal conductivity, low thermal expansion coefficient and high optical bandgap over the last decade, have proved their indispensable roles in a wide range of applications. Hexagonal boron nitride (h-BN), a layered material having a high thermal conductivity along the planes and the band gap of 5.9 eV, has always been a promising candidate to provide superior heat transfer with minimal phonon scattering through the system. Hence, extensive researches have been devoted to improving the thermal conductivity of different matrices by using h-BN fillers. Apart from that, lubrication property of h-BN has also been extensively researched, demonstrating the effectivity of this layered structure in reduction of friction coefficient, increasing wear resistance and cost-effectivity of the process. Herein, an in-depth discussion of thermal and tribological properties of the reinforced composite by h-BN will be provided, focusing on the recent progress and future trends.

Keywords: hexagonal boron nitride (h-BN); 2D materials; composite; thermal properties; thermal conductivity; tribological properties; coefficient of friction; wear resistance

1. Introduction

The rise of graphene in 2004 [1] followed by an in-depth interpretation of the thin carbon film properties has provoked an exhaustive search on other alternative two-dimensional (2D) materials due to their newly emerged size-dependent privileges in properties and structures [2,3]. Owing to the development of efficient structural manipulation approaches, the fast growing list of 2D materials are no longer limited to graphene and can be expanded to metal oxides/hydroxides [2,4,5], transition metal carbides and nitrides (MXenes) [6,7], transition metal dichalcogenides (TMDs) [8,9], and h-BN [10]. Among this family, 2D h-BN with high structural resemblance with graphene has gravitated considerable attention and is so-called as "white graphene".

h-BN bulk is a layered material consisting of individual basal planes known as BN nanosheet (BNNS). Each layer is comprised of alternative boron (B) and nitrogen (N) atoms partially-covalent bonded in a honeycomb (sp^2) configuration [10,11]. Due to the electronegativity difference between B and N atoms (N = 3.04 and B = 2.04 [12]), an ionicity also permeates within the 1.44 Å B-N bond distorting the electronic states symmetry. Then it reflects a severe lack of delocalized Pz electrons in both Valance and Conduction bands and subsequent generation of a large band gap of 5.1–5.9 eV [12,13]. Moreover, possessing ultra-flat atomic surface and a negligible lattice constant mismatch with graphene (1.7%) [14] can idealize them being an ideal supporter for graphene-based nanoelectronics bearing superior chemical and thermal stabilities [10,15,16]. Furthermore, the outstanding oxidation/corrosion resistance of h-BN layers as a capping layer and/or dielectric provide an opportunity to protect the susceptible substances from any chemical/structural damages [17,18]. Being an electric insulator also paves a way for further optoelectronic applications such as ultraviolet light-emitters [10,17]. Recent efforts on bandgap tunability of h-BN through doping or chemical functionalization has also revealed their potential for a wide range of electrochemical applications, from energy storage to biosensors [19–25].

Apart from all these excellences, high in-plane thermal conductivity (TC) of h-BN is capable of improving heat dissipation in many applications. Therefore, fabrication of various composites having h-BN as a thermal conductive filler is now highly demanded due to simultaneous provision of high TC along with high chemical and mechanical stabilities. As an example, in electronic packaging industries with polymeric materials, longevity and reliability of electronic devices increase when heat dissipation is well-controlled [26,27]. Furthermore, due to layered structure and weak van der Waals interactions between the adjacent layers, h-BN is considered as an extensively-used lubricant material [11]. Therefore, its low shear strength and capability to preserve the lubrication capability at elevated temperatures or in oxidative environments has gained numerous attentions in improving wear resistance of durable polymer/metal/ceramic matrix tribo-composites in both dry and wet media [28,29].

Despite all the researches and publications on the TC and tribological properties of BNNSs-reinforced composites, there has been not a comprehensive article covering all aspects of this trend. Herein, in the second chapter, we discussed fundamental thermal conductivity theories with focus on 2D h-BN and conveying h-BN's superior thermal properties to polymer matrix composite (PMC) through various synthesis techniques. In the third chapter, we elaborated basics of tribological properties relevant to h-BN all the way up to its applicability in tribological applications.

2. Thermal Properties

2.1. Conductivity Theory

Generally, heat energy transfer occurs through three different pathways: radiation, convection, and conduction. In a solid-state material, thermal conduction is the dominant mechanism. According to a fundamental point of view, thermal energy appears as vibrational energy in materials, thereby, the transfer of a particle's vibrational energy to the neighboring particles without moving the location of matter is called thermal conduction. Heat diffusion mechanism within a solid material stems from two contributions: (1) atoms collisions and interactions known as wave-like phonon conduction and (2) electron movements. TC of metals basically originates from energized electrons, while phonon conduction is dominant in nonmetallic systems [30]. Thermal energy in crystalline systems such as metals, 2D materials including graphene, h-BN, and etc. disseminates through harmonized vibrational waves, causing simultaneous vacillation of whole particles with the same frequency. Figure 1a clearly portrayed the heat transfer mechanism into a crystalline material from surface heat absorption to heat conduction/radiation to surroundings. However, structural discontinuities such as defects, grains boundaries, and dislocations induce heterogeneity to the structure that ultimately are disturbing particles harmonic vibrations. The result of this inharmonious vibration is phonon scattering, a phenomenon that phonon conduction is not transferred by using a unique vibrational

wave through the material. Moreover, phonon scatterings inevitably induce thermal resistance called "Kapitza resistance". Unlike ideal crystalline materials, amorphous materials such as polymers, intrinsically have a combination of structural discontinuities including chain folding and chain ends due to the absence of long-range ordered structure. Therefore, they suffer from disordered vibrations throughout the chains (Figure 1b) and possessing decelerated heat transfer compared to crystalline systems. To understand the difference between heat transfer mechanisms of crystalline and amorphous structures, they are often resembled to a Newton pendulum shown in Figure 1c,d. The ordered crystalline structure quickly disseminates the starting vibration to the other side, while the same vibration should be propagated throughout the entire chain in an amorphous structure, leading to inharmonious vibration and delayed heat transfer [12,30].

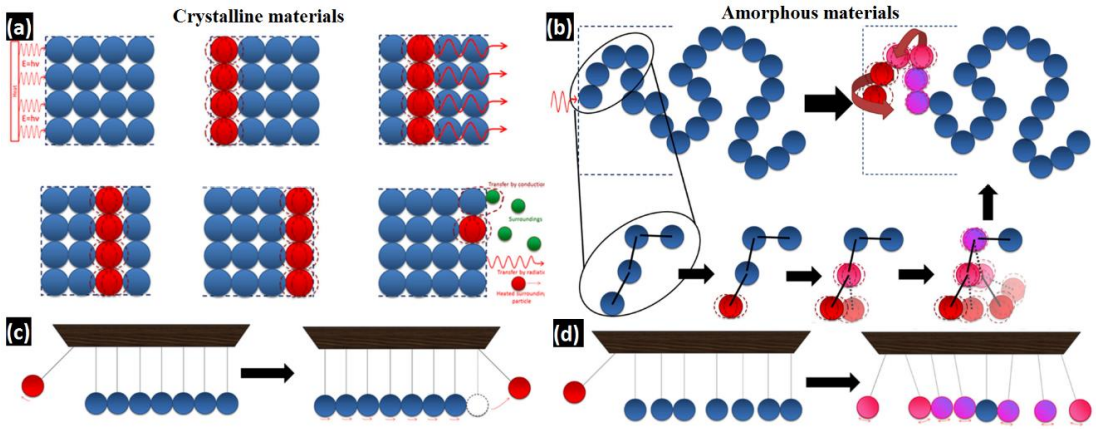

Figure 1. Heat transfer mechanism in (**a**) crystalline and (**b**) amorphous (polymer) materials; representation of difference in heat transfer mechanism of (**c**) crystalline and (**d**) amorphous (polymer) materials via Newton pendulum models (Reprinted with permission from Elsevier, Copyrights 2016) [30].

TC is considered a material's capacity in conducting heat through a certain thickness of material, perpendicular to the surface area and during a certain amount of time as a result of imposing temperature gradient to the opposite surfaces. All these parameters which play decisive roles in TC's value are hidden within its mathematical equation shown below as Equation (1):

$$k = \alpha \times C_p \times \rho \tag{1}$$

where k is TC (W $m^{-1} \cdot K^{-1}$), C_p is the specific heat capacity (the amount of heat required to elevate the temperature of a material by 1 °C, J $kg^{-1} \cdot K^{-1}$), ρ is the material's density ($kg \cdot m^{-3}$), and α is thermal diffusivity (speed of the transferred heat through the material, m^2 s^{-1}). In isotropic materials, heat conduction occurs uniformly irrelevant to the direction, while in anisotropic materials like composites in which properties are under the influence of direction, TC depends on the direction of heat flux. Thereby, TC is determined by a tensor being a function of particles orientations and corresponding directions within the composite.

$$k_{x,\,y,\,z,\,T} = \begin{pmatrix} k_{xx} & k_{xy} & k_{xz} \\ k_{yx} & k_{yy} & k_{yz} \\ k_{zx} & k_{zy} & k_{zz} \end{pmatrix} \tag{2}$$

Finally, the following equation is the correct form of TC in anisotropic systems [12,30]:

$$\begin{aligned} k_{xx}\frac{\delta^2 T}{\delta x^2} + k_{yy}\frac{\delta^2 T}{\delta y^2} + k_{zz}\frac{\delta^2 T}{\delta z^2} + \left(k_{xy} + k_{yx}\right)\frac{\delta^2 T}{\delta x \delta y} + \left(k_{yz} + k_{zy}\right)\frac{\delta^2 T}{\delta y \delta z} + \left(k_{xz} + k_{zx}\right)\frac{\delta^2 T}{\delta x \delta z} \\ = \rho \times C_p \times \frac{\delta T}{\delta t} \end{aligned} \tag{3}$$

2.2. Thermal Properties of h-BN

In the recent decade, layered bulk h-BN as an anisotropic material has gained considerable attentions towards the thermal management of electronic devices, mainly due to its high in-plane (parallel to its basal plane) TC of 600 W m^{-1}·K^{-1}. The anisotropy of h-BN stems from strength difference between strong covalent bonds within hexagonal planes of h-BN (intralayer) and weak van der Waals forces which attach the adjacent BNNSs (interlayer) [31]. Therefore, most of h-BN's properties are direction-dependent, known as anisotropic. Being an intrinsic anisotropic material makes the h-BN's out-of-plane (perpendicular to its basal plane) TC at least 1–5 W m^{-1}·K^{-1} and at most 30 W m^{-1}·K^{-1} [32,33]. Besides its high in-plane TC, high surface area with atomic flatness provides a platform to dissipate heat without formation of localized hot spots [32,33]. Based on theories of TC, reduced layer numbers and the absence of weak van der Waals interlayer interactions subsequently reduce the phonon-phonon scattering. Therefore, in the absence of experimental results from direct measurements of TC values of h-BN's monolayers, we can rely on theories that h-BN monolayers possess significantly higher TC value than their multilayered, bulk counterparts due to the reduction of phonon-phonon scattering in the 2D structure. According to numerical results of the phonon Boltzmann transport equation, a theoretical TC value of >600 W m^{-1}·K^{-1} is calculated for h-BN monolayer which is higher than the calculated value for multilayered, bulk h-BN (400 W m^{-1}·K^{-1}). Besides phonon-phonon scattering, the out-of-plane vibration can also determine the TC value in multilayer h-BN. To be more specific, interlayer interaction in multilayer h-BN leads to a significant reduction in the TC value compared to monolayer h-BN [2,10,34].

2.3. Fabrication of h-BN-Reinforced Polymer-Based Composites

Highly demanded miniaturization of electronic devices along with their multi-functionality necessitates a systematic control on heat dissipation to enhance the longevity and reliability. In general, the responsibility of heat dissipation is appointed to polymer matric composites, known as electronic packaging materials, which possess high TC while being dielectric [26,27,35]. To meet the required features for real-time practicality, highly thermal conductive fillers such as ceramic fillers h-BN, silicon carbide (SiC) [36,37], silicon nitride (Si_3N_4) [38], aluminum nitride (AlN), aluminum oxide (Al_2O_3) [39]), carbon-based fillers (carbon nanotube (CNT) [40], graphene [41], diamond [42], carbon fiber [43]), and metal fillers (silver nanowires [44], copper [45], aluminum [46]) have been extensively used to yield thermally conductive polymer composites. High electrical conductivity of carbon-based materials, metal oxides, and metals as fillers also increases the electrical conductivity of the final composite, leading to delayed signal propagation in electronic devices and restrict their application in electronic industry. Among ceramic fillers, h-BN has high TC, high chemical stability, large aspect ratio while possessing lowest dielectric constant among ceramic fillers (~4) and being a perfect electrical insulator ($\sigma = 10^{-11}$ S·cm^{-1}) due to its large band gap. Therefore, all these merits turn h-BN into a promising candidate for utilization in electronic packaging materials [32,47–50]. Since h-BN is regarded as an anisotropic filler with distinctive difference in its in-plane and out-of-plane TCs, the TC of the h-BN-reinforced polymer composite is also affected by filler's orientation, filler-filler and filler-polymer interfacial properties [51]. Thereby, many efforts have been devoted to controlling the orientation of h-BN platelets through synthesis techniques to exploit the ultimate potential of its high TC in polymer composites. In the following, a wide range of synthesis methods focused on orientation manipulating and incorporation of h-BN fillers into various polymer matrices are discussed.

2.3.1. Freeze-Drying

Freeze-drying is regarded as one of the effective methods in constructing 3D oriented inner structures which is capable of maintaining the as-generated structure during the ice-nucleation stage. In an interesting work, a 3D nacre-shaped thermal conductive network based on BNNSs/epoxy composite was fabricated through a bidirectional freezing technique, as shown in Figure 2a [52].

For this purpose, an aqueous slurry of mechanically exfoliated BNNSs and polyvinyl alcohol (PVA) was placed into a freezing mold equipped with a polydimethylsiloxane (PDMS) wedge to generate temperature gradient in both the vertical and horizontal directions. Ice nucleation in a lamellar pattern as a result of bidirectional freezing ultimately rendered a 3D lamellar structure of BNNSs/PVA aerogels. The freeze-dried BNNSs/PVA aerogels were followed by epoxy resin infiltration and curing to obtain BNNSs/epoxy composite. Scanning electron microscopy (SEM) evaluations (Figure 2b,c) revealed that the highly ordered, aligned lamellar nacre-shaped network remained intact even after resin infiltration, leading to high TC due to providing prolonged phonon pathways. In a similar work [53], a freeze-dried BNNSs foam was hybridized with PDMS to manufacture a flexible phonon transmitter composite. The method's superiority lies in the carbonization welding process, which assures the physical structure of the freeze-dried BNNSs foam and favors its static charges' dissipation. As shown in Figure 2d, anisotropic BNNSs foam was synthesized by directional freezing of a chitosan/BNNSs dispersion followed by vacuum freeze-drying for 48 h at −50 °C. Afterward, the as-obtained BNNSs foam underwent carbonization at 800 °C for 0.5 h. At last, the BNNSs foam was immersed into PDMS resin to construct a thermal conductive network. Morphological assessments clearly confirmed highly ordered BNNSs walls formed along with the as-grown ices. Upon post-treatment carbonization welding, well-connected BNNSs walls with the distance of ~50 µm (3.0 vol.% BNNSs) were achieved. Even after PDMS infiltration, the order of BNNSs foam is intact with no trace of pores, implying the successful resin immersion (Figure 2e,f).

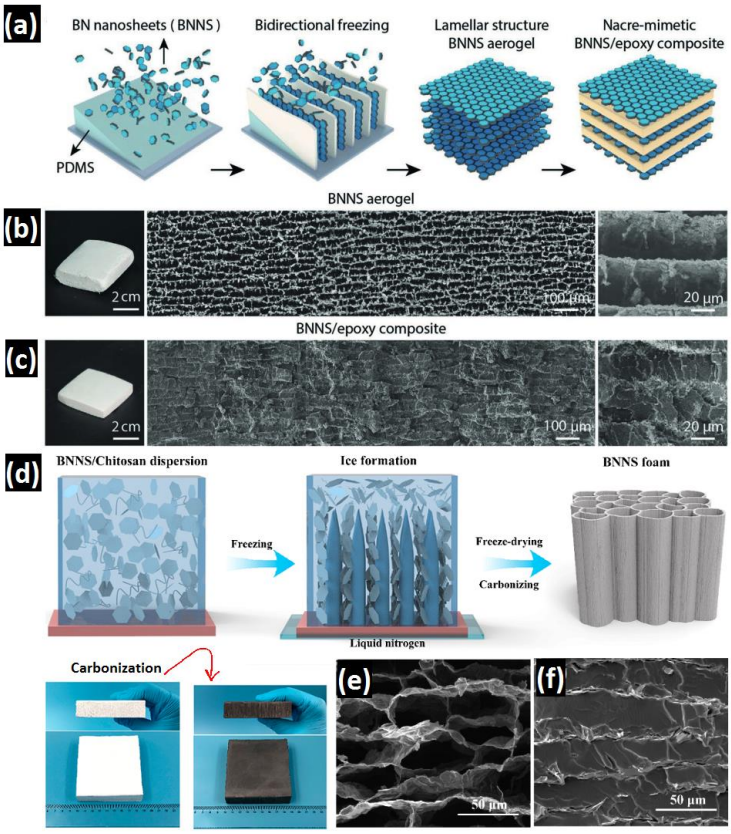

Figure 2. (**a**) Schematic illustration of bidirectional freezing technique of BN nanosheets (BNNSs) aerogels/epoxy composite followed by epoxy resin infiltration, optical, surface and cross section SEM images of (**b**) BNNSs aerogel and (**c**) BNNSs/epoxy composite (Reprinted with permission from WILEY-VCH, Copyrights 2019) [52]. (**d**) Schematic illustration of directional freezing and freeze-drying of chitosan/BNNSs, Cross section SEM images of (**e**) BNNSs foams and (**f**) phonon transmitter BNNSs/PDMS composite (Reprinted with permission from the American Chemical Society, Copyrights 2019) [53].

Manipulation of BNNSs to meet the requirement of a lightweight 3D conductive network with both outstanding thermal and mechanical performance is quite challenging in the electronic industry. However, a superelastic, lightweight nanocomposite based on 3D h-BN/Polyimide (PI) aerogels was constructed based on facile and green freeze-drying method [54]. Firstly, BNNSs was obtained by mechanical exfoliation of h-BN in the presence of D-glucose and nitrogen in a steel milling container. Prior hybridization with PI, the resultant hydroxyl-functionalized BNNSs were dialyzed for 1 week to eliminate any trace of D-glucose. The well-stirred BNNSs and poly (amic acid) (PAA) suspension was exposed to freeze-drying process at −20 °C for 48 h. Finally, the as-synthesized aerogels were transferred to N_2 atmosphere tube furnace under accurate time and temperature schedule to gain thermally cross-linked BNNSs/PI aerogels (Figure 3a). During synthesis, two main factors including the interaction between hydrogen bonding of the functionalized h-BN and intrinsically oxygen, nitrogen-containing groups of PPA, and the π-π interaction between the B-N layer of h-BN and benzene ring of PPA backbone are responsible for the improved adhesion between these two components. According to the morphological evaluations, the functionalized BNNSs possessed lateral size of 200 nm with 3–9 atomic layers. After hybridization, the morphological assessments revealed a honeycomb-shaped network fulfilling its superelasticity and stretchability, as shown in Figure 3b,c. In addition, the BNNSs possessed highly aligned structures, parallel to PI layers, causing an inorganic-organic binary network. Its unique superelasticity accompanied by considerable hydrophobicity provides a platform to be utilized in any desired shape in harsh environments.

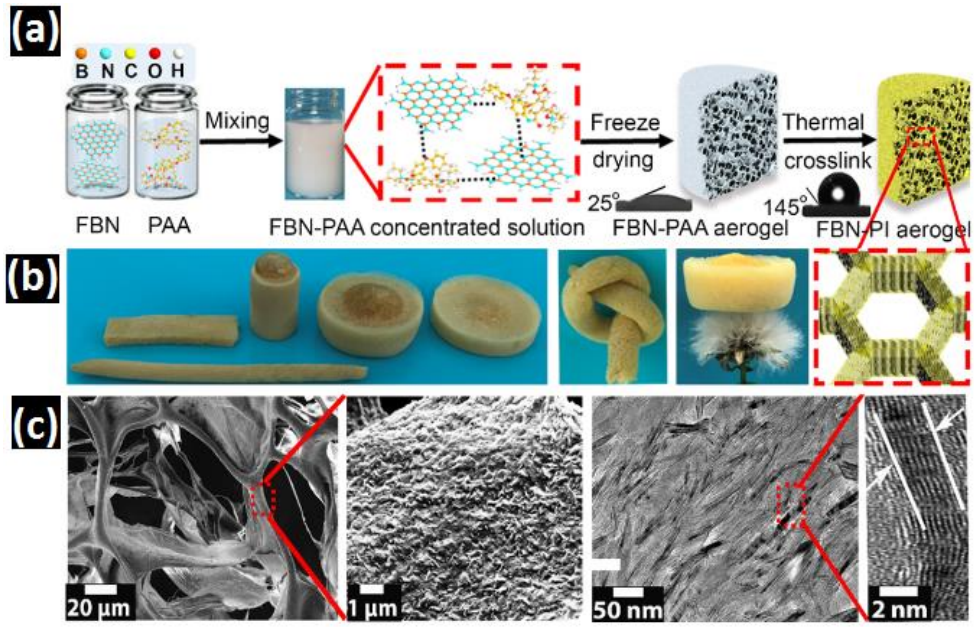

Figure 3. (**a**) Schematic illustration of fabrication procedure, (**b**) photographs of superelasticity and lightweight characteristics of the composite with taking various shapes and knots, and (**c**) morphological images of BNNSs/PI aerogels composite (Reprinted with permission from the American Chemical Society, Copyrights 2019) [54].

2.3.2. Template-Assisted

Achieving a continuous high TC in both out-of-plane and in-plane direction is challenging for bulk layered materials. Based on recent studies, a 3D segregated filler structure has shown to be promising in supplying uniform TC over both directions [55–57]. As an example, integration of a 3D segregated structure of h-BN fillers with epoxy resin has been shown capable of enhancing TC [58]. For this purpose, h-BN microbeads (BNMBs) were formed via a facile salt-template method in which NaCl recrystallization and PVA presence as cohesive agents hold h-BN nanoparticles together to form spherical agglomerates. Consecutively, washing away NaCl templates in cold water, drying, and resin

infiltration led to the formation of segregated BNMBs/epoxy composite. Four evaporation stages of the salt-template technique are as follow:

1. Over-saturated NaCl solution as a result of water evaporation embarks NaCl recrystallization on the surface of h-BN; PVA, as a binding agent, fixes recrystallized NaCl particles on h-BN surface. Then the PVA/NaCl/h-BN mixture gradually becomes flocculated.
2. Flocculated seeds are accumulated, enlarge to minimize surface free energy, leading to the formation of primary BNMBs particles.
3. By losing more water, more NaCl/h-BN particles joined the primary particles, giving rise to the formation of spherical secondary BNMBs particles.
4. Upon template removal through cold water, the recrystallization is exterminated and hollow BNMBs can be obtained.

Customizing continuous heat conductive structure through template-assisted method is still an obstacle in electronic packaging industries. However, continuous and connected large and small sizes of BNNSs coupled with thermoplastic polyurethane (TPU) have recently been introduced as a rapid heat transfer composite [59]. For this purpose, ultrasonic exfoliated large and small BNNSs (L- BNNSs and S-BNNSs, respectively) were mixed with N,N-dimethylformamide (DMF) and 90 wt.% TPU. The resultant mixture was transferred into Teflon dished to evaporate DMF gradually until it gets dried, as shown in Figure 4a. According to morphological evaluations, BNNSs are dispersed evenly within the TPU matrix with good contact compatibility, enhancing the overall TC (Figure 4b). As a result of template evaporation, adjacent L-BNNSs are connected to deliver a continuous, conductive pathway and S-BNNSs filled the gaps between them to construct an interconnected percolation network (Figure 4c).

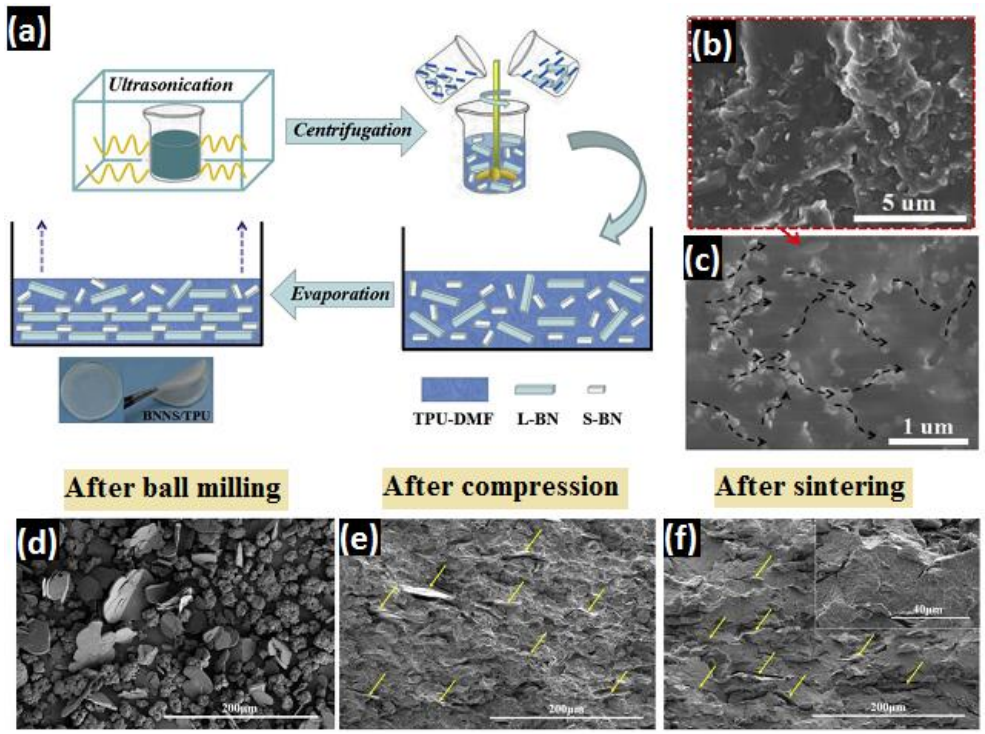

Figure 4. (**a**) Schematic illustration of self-assembly evaporation of flexible L and S-BNNSs/TPU composite, (**b**,**c**) SEM images of 10 wt.% BNNSs/TPU (Reprinted with permission from Elsevier, Copyrights 2019) [59]. SEM images of 30 wt.% h-BN/PI composite after (**d**) ball milling, (**e**) high-pressure compression, and (**f**) low-temperature sintering (Reprinted with permission from Elsevier, Copyrights 2019) [60].

2.3.3. Mechanical Milling

To harness the highest potential of h-BN's high in-plane TC, alignment of h-BN platelets towards one direction seems a promising solution. In a recent work [60], the insoluble and non-melting characteristics of PI are exploited to fabricate highly in-plane aligned h-BN/PI composite by a facile and controllable method known as ball milling, high-pressure compression and low-temperature sintering. SEM images of post-milling demonstrate that the h-BN platelets are uniformly dispersed within polymer matrix made of spherical PI particles (Figure 4d). By optimizing h-BN content to 30 wt.%, PI particles wearing is minimized due to lubrication characteristic of h-BN protecting them against wear deterioration and ultimately, preserves the original sizes. High in-plane alignments of the incorporated h-BN platelets can be seen clearly in SEM cross-section image of half-finished samples after high-pressure compression (Figure 4e). Since the compression stage is crucial in inducing in-plane orientation, low-temperature sintering at 290 °C can create well-coalesced PI particles and a complete plasticization of the composite, as shown in Figure 4f. Therefore, a complete heat conductive network is prepared, confirming ameliorated TC of h-BN/PI composite.

Being an anisotropic filler has made h-BN capable of producing various TC properties in different directions. Since heat dissipation between heat sinks and electronic devices majorly happens in vertical direction, thus, out-of-plane TC takes precedence over in-plane TC. Producing vertically aligned h-BN structure can be carried out by a variety of techniques including freeze-drying [52,61], electrically/magnetically induced alignment [62] as well as straightforward mechanical two-roll milling approach. For instance, a research work [63] focused on two-roll milling technique to fabricate vertically aligned h-BN/silicon rubber (SR) composite. As illustrated in Figure 5a, a mixture of h-BN/SR is sheared five times by a two-roll milling machine with the rolling distance of 0.35 mm to obtain a monolithic aligned h-BN/SR composite sheet. Subsequently, the as-obtained sheet is cut off perpendicular to the shear direction, lined the as-cut pieces up vertically, and cured at 170 °C in a hydraulic hot press to deliver vertically aligned h-BN/SR composite. SEM images, shown in Figure 5b, display the well-dispersed and well-vertically aligned h-BN sheets with the thickness of ~300 nm and diameter of ~10 μm within SR matrix. In an alternative work [64], the synergistic effect of binary hybrid filler was exploited to construct a BNNSs-reinforced silicon thermal grease (STG) composite. As shown in Figure 5c, the hybrid filler is firstly prepared by self-assembly of BNNSs on the surface of reduced graphene oxide (RGO) in the presence of PVA as a polymeric binder. The adhesive characteristic of PVA not only bonds BNNSs together in clusters, but also adheres those formed clusters to the surface of RGO efficiently. The dried RGO/h-BN precursor then is grinded in a planetary ball mill followed by pyrolization in a tube furnace with argon atmosphere to remove polymeric binder and obtain 3D RGO/h-BN stacking structure. The final thermal interface material (TIM) is prepared by shearing a mixture of RGO/h-BN and STG resin 6–9 times in a three-roller machine, the as-synthesized 3D RGO/h-BN stacking composite with the lateral size of 11 μm in which graphene is encircled by BNNSs clusters is confirmed by SEM assessment (Figure 5d,e).

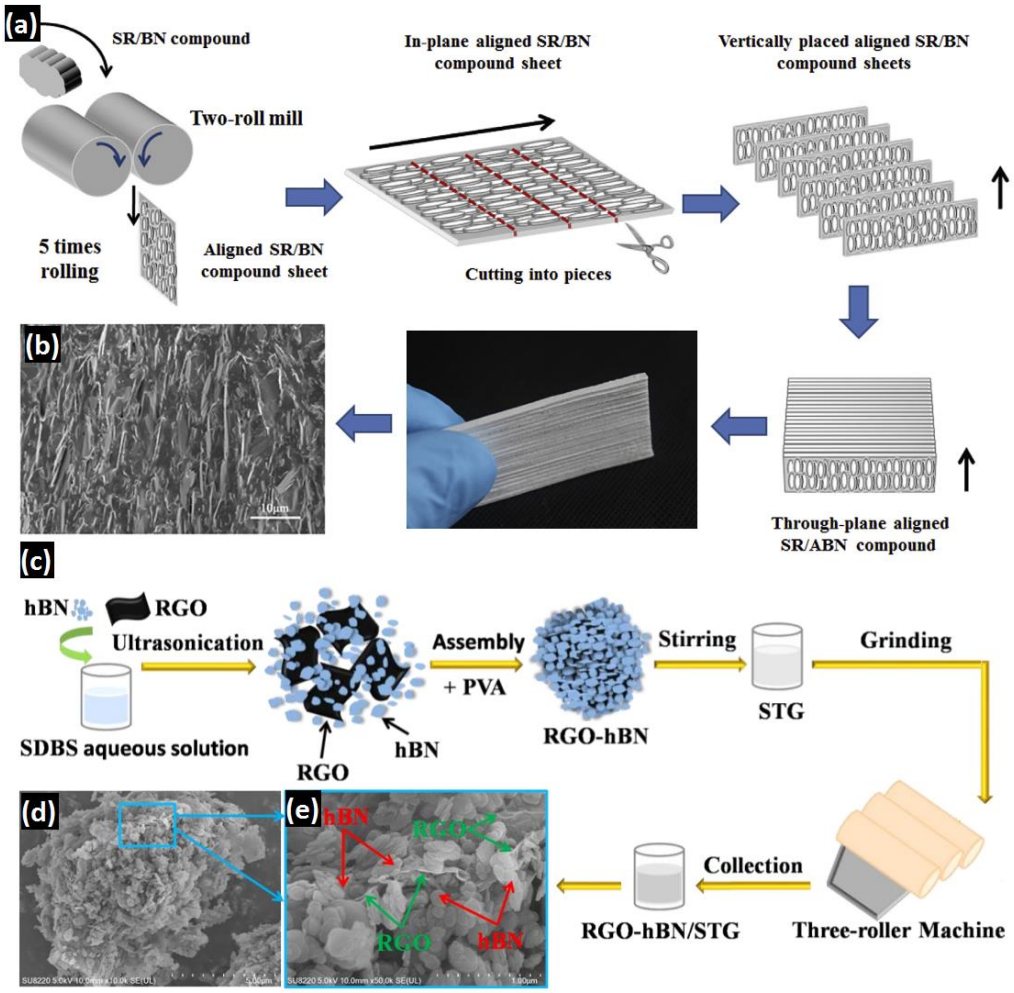

Figure 5. (**a**) Schematic presentation of two-roller milling fabrication process of vertically aligned h-BN/SR composite, (**b**) SEM image of 30.6 vol.% h-BN/SR (Reprinted with permission from Elsevier, Copyrights 2019) [63]. (**c**) Schematic illustration of self-assembly, three-roller milling technique of BNNSs/RGO/STG composite, (**d**,**e**) SEM images of BNNSs/RGO (Reprinted with permission from MDPI, Copyrights 2019) [64].

2.3.4. Magnetic/Electric-Field Assisted

A common approach to intensify the TC of TIMs is loading high amounts of BNNSs fillers into a polymer matrix, although it may deteriorate the mechanical properties of the final composite. Recently, vertical configuration of BNNSs has shown obviating usage of high amounts of filler loading, with flexibility lost in the obtained TIM [65–67]. Thereby, magnetic/electric fields are considered high efficiency and cost-effective techniques to yield vertically aligned BNNSs phonon transmission networks. In a recent work [62], a flexible TIM was designed based on magnetic-assisted vertically aligned BNNSs/PDMS composite with the assistance of FeCo magnetic nanocubes. To deliver well-oriented heat conduction channels, surface modification was firstly applied separately for FeCo nanocubes and h-BN powder to generate positively charged poly (diallyldimethylammonium chloride) (PDDA)@FeCo nanocubes and negatively charged BNNSs. Then, the strong electrostatic interactions between these two opposite-charged particles in the self-assembly process produced FeCo-BNNSs complex nanomaterials. To obtain FeCo-BNNSs/PDMS composite, a mixture of dried FeCo-BNNSs nanoparticles and PDMS resin was transferred to a spray gun and spray-coated on a hydrophobic glass substrate. At last, the spray-coated substrate was placed amid two vertically aligned rare permanent magnets with the field intensity of 35 mT for 1.5 h to orientate BNNSs platelets in the vertical direction (Figure 6a). The response of the as-synthesized FeCo-BNNSs complex to external magnetic field is

clearly demonstrated in Figure 6b. During the self-assembly stage, the {001} facets of BNNSs were attached firmly to the {001} facets of PDDA@FeCo magnetic nanocubes. Upon applying a vertical magnetic field, FeCo nanocubes can easily orientate along {001} as an easy magnetization direction and accordingly, BNNSs platelets accompany FeCo in this magnetic-assisted orientation. The successful vertical orientation of BNNSs in the PDMS composite is displayed in Figure 6c.

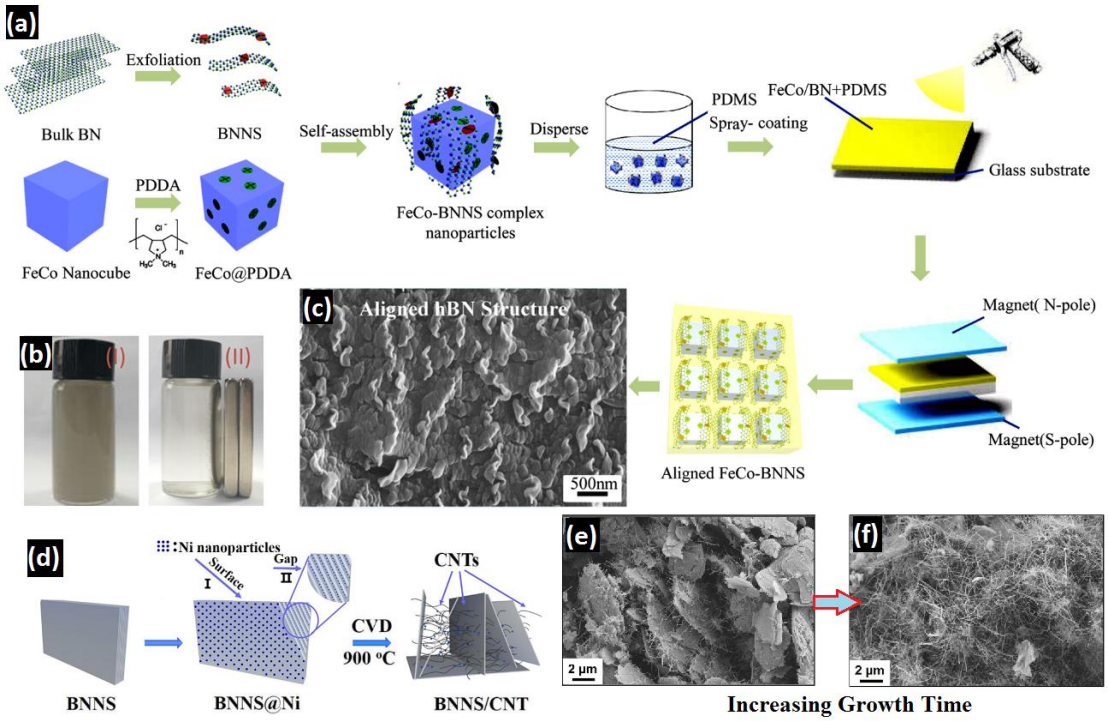

Figure 6. (**a**) Self-assembly and magnetic-assisted techniques in synthesizing vertically aligned BNNSs/PDMS composite, (**b**) response of FeCo-BNNSs complex to external magnetic field, (**c**) SEM image of vertically aligned BNNSs vi the help of magnetic FeCo nanocubes (Reprinted with permission from the American Chemical Society, Copyrights 2019) [62]. (**d**) In-situ growth of CNTs on the surface of BNNSs by CVD rout, (**e**,**f**) SEM images of CNT/BNNSs hybrid filler under increasing growth time (Reprinted with permission from Elsevier, Copyrights 2019) [68].

2.3.5. Other Synthesis Methods

Taking benefit from the synergistic effect of 3D hybrid fillers in heat dissipation, chemical vapor deposition (CVD) grown-carbon nanotubes (CNTs) on the surface of BNNSs has also been coupled with epoxy resin to produce a high TC TIM [68]. For this purpose, catalyst-loaded BNNSs are prepared by ultrasonication of a certain amount of BNNSs and nickel acetate, vacuum drying, and grinding to yield well-dispersed catalyst-BNNSs. In-situ CVD growth then is carried out in two stages: (1) the catalyst-loaded BNNSs exposure to 500 °C under the flow of mixed argon and hydrogen gases for 1 h to reduce nickel acetate to nickel nanoparticles (Figure 6d), (2) the temperature is raised to 900 °C and methane gas as carbon source was pumped into the quartz furnace. The CNTs growth time should then be adjusted between 30-120 min. At last, CNTs/BNNSs/epoxy resin is prepared in a high-shear mixer followed by curing at 130 °C. Morphological evaluations in Figure 6e,f revealed that long CNTs under prolonged growth time grew between BNNSs in an interesting way that connected those sheets together, producing a continuous CNTs/BNNSs thermal conduction network. In addition, the as-grown CNTs are mainly multi-walled CNTs with outer diameters of 10–50 nm.

Using the same CVD technique, an interesting 3D network based on BNNSs-reinforced graphene tube woven fabric (GTWF)/PDMS composite was fabricated with remarkable in-plane TC. Inexpensive Ni fabrics used as a growth substrate and graphene tubes were grown on its surface under the flow of methane gas in a quartz tube furnace to obtain GTWF-Ni fabric. Upon etching Ni in an etching

solution ($HCl:FeCl_3$), pure GTWF was achieved. Eventually, BNNSs/GTWF/PDMS composite was prepared by infiltration of BNNSs/PDMS mixture into five layers of stacked GTWF and cured at 80 °C, as depicted in Figure 7a. The morphological changes from pristine Ni substrate to as-synthesized BNNSs/GTWF/PDMS composite are shown in Figure 7a, confirming the successful hybridization of these three components in one TMI. In an alternative work, the combination of electrospinning and vacuum-assisted impregnation was utilized to construct a flexible TIM based on an interconnected and vertically aligned BNNSs/PVA/PDMS composite [69]. Firstly, a PVA supported BNNSs was prepared via electrospinning technique on an aluminum foil with the working voltage of 16 kV. Then, the as-synthesized PVA/BNNSs film was cut into narrow strips with the size of 15 mm, as shown in Figure 7b. All the obtained strips were rolled up perpendicular to the direction of the electrospun fibers in a way that the next strip got engaged with the previous one to construct a PVA/BNNSs cylinder with the diameter of 15 mm. At last, the as-ready cylinder was impregnated with PDMS resin under vacuum and followed by curing at 100 °C for 1 h. According to the morphological examinations, electrospun PVA/BNNSs fibers possessed a highly vertical ordered structure in which BNNSs adhered to the PVA fibers so tightly (Figure 7c,d). This strong bond between PVA and BBNSs originates from amino and hydroxyl groups of BNNSs which facilitated its dispersion in PVA solution and interacted with PVA through strong hydrogen bonding. This strong hydrogen bonding is responsible for the well-stacked and interconnected BNNSs which were assembled on the surface of PVA fibers, resembling a fallen domino. This in-plane overlapping connection is expected to drastically decrease the interfacial thermal resistance within the PVA/BNNSs fibers. Eventually, the PDMS resin was fully filled the pores and gaps of PVA/BNNSs cylinder and no debonding was occurred between fibers and polymer matrix.

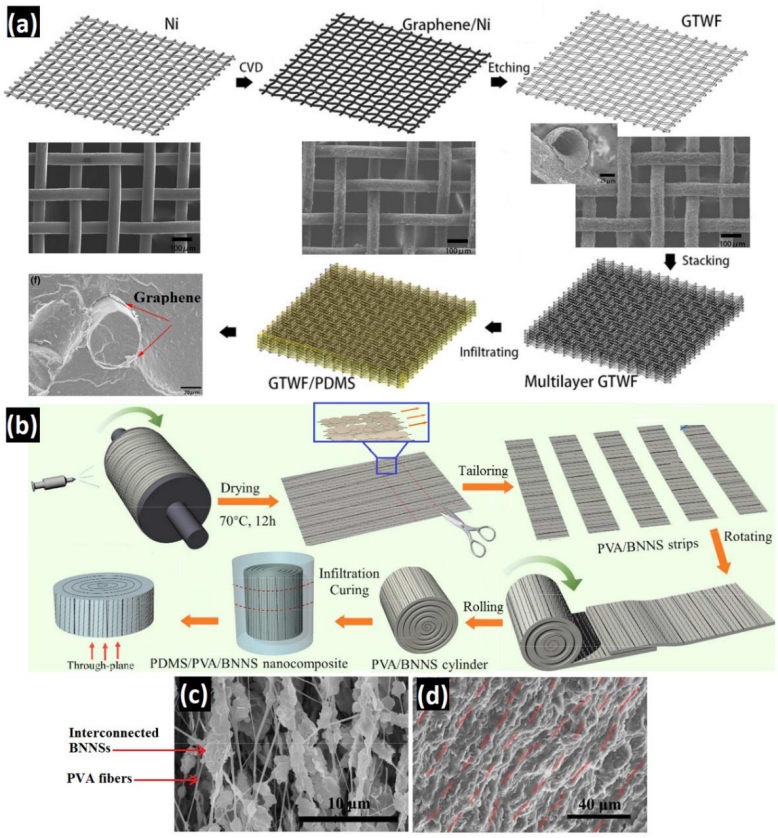

Figure 7. (**a**) Schematic illustration and SEM images of BNNSs/GTWF/PDMS composite (Reprinted with permission from WILEY-VCH, Copyrights 2019) [33]. (**b**) Electrospinning and vacuum impregnation preparation of BNNSs/PVA/PDMS composite, (**c**,**d**) SEM images of electrospun BNNSs/PVA with interconnected structure (Reprinted with permission from the American Chemical Society, Copyrights 2017) [69].

2.4. Thermal Conductivity Evaluations of h-BN-Reinforced Polymer Composites

According to theoretical studies, it is possible to exploit the ultimate potential of h-BN's TC within a hybrid composite if the phonon-phonon scattering within its 2D structure is overcome. Agari et al. suggested a mathematical model to define the TC of filler-reinforced PMC [70]:

$$\log k_{Composite} = V_{h-BN} \times C_{h-BN} \times \log\left[\frac{k_{h-BN}}{C_{polymer} \times k_{polymer}}\right] + \log\left(C_{polymer} \times k_{polymer}\right) \quad (4)$$

where $k_{composite}$ is the overall TC of the polymer composite, $k_{h\text{-}BN}$ is the TC of h-BN fillers, and $k_{polymer}$ is the TC of polymer matrix; $V_{h\text{-}BN}$ is the volume content of incorporated h-BN fillers. $C_{h-BN} \times \log\left[\frac{k_{h-BN}}{C_{polymer} \times k_{polymer}}\right]$ term is the effect of hybridization on the quality of h-BN's heat conduction, explaining how the TC of polymer matrix limits the TC of h-BN fillers while $\log\left(C_{polymer} \times k_{polymer}\right)$ term unfolds how the crystallinity of polymer matrix changes upon incorporation of h-BN fillers. $C_{polymer}$ and $C_{h\text{-}BN}$ are considered as specific heat capacities. $k_{h\text{-}BN}/k_{polymer}$ ratio in the former term is known as "decreased TC of h-BN fillers", expounding how much the TC of h-BN fillers within the polymeric matrix is lower than the TC of pristine h-BN fillers. Since the polymer matrix affects the TC of its incorporated h-BN fillers, this ratio actually implies that polymer matrix is like an impediment against heat conduction [12,30].

2.4.1. h-BN as a Single Filler

Recently, a flexible BNNSs/PDMS composite having a 3D network structure was fabricated via a two-step method of freeze-drying and carbonizing. The resulting 3D BNNSs/PDMS with 15.8 vol.% showed a prominent TC of 7.46 W $m^{-1} \cdot k^{-1}$ which was enhanced by 3900% compared to neat PDMS. This improvement mainly stems from the dominant thermal transport channels formed through the polymer matrix. Plus, the residual carbon remaining in the composite structure led to a tremendous antistatic behavior and preserved the composite from dust and destruction. Figure 8a,b illustrated the comparison of surface resistivity and volume resistivity of Random PDMS and 3D BNNSs/PDMS. Both parameter values are dropped down in the 3D-BNNSs/PDMS composite, which shows that the residual carbon in the PDMS matrix formed a conductive network, leading to the anti-static performance and preserves the composite from dust and destruction. The schematic of this mechanism is shown in Figure 8c. A more comprehensible image of this feature is represented in Figure 8d,e by comparing the charge dissipation ability of Pure PDMS, Random BNNSs/PDMS, and 3D-BNNSs/PDMS samples. The conductive network in 3D-BNNSs/PDMS composite depletes the accumulated surface static charges immediately, while the Random BNNSs/PDMS sample adsorbed the most significant portion of Polystyrene spheres owing to its high surface resistivity. Figure 8f highlights the developed thermal performance of the 3D network composite compared with the random structure. In the 3D-BNNSs/PDMS composite, the neighboring BNNSs are welded together and brought efficient phonon pathways, so that the heat dissipation can occur faster. Yet, the phonon scattering at the random BNNSs and PDMS interfaces is more likely due to the absence of functional heat conductive channels, causing a deficient heat dissipation behavior [53].

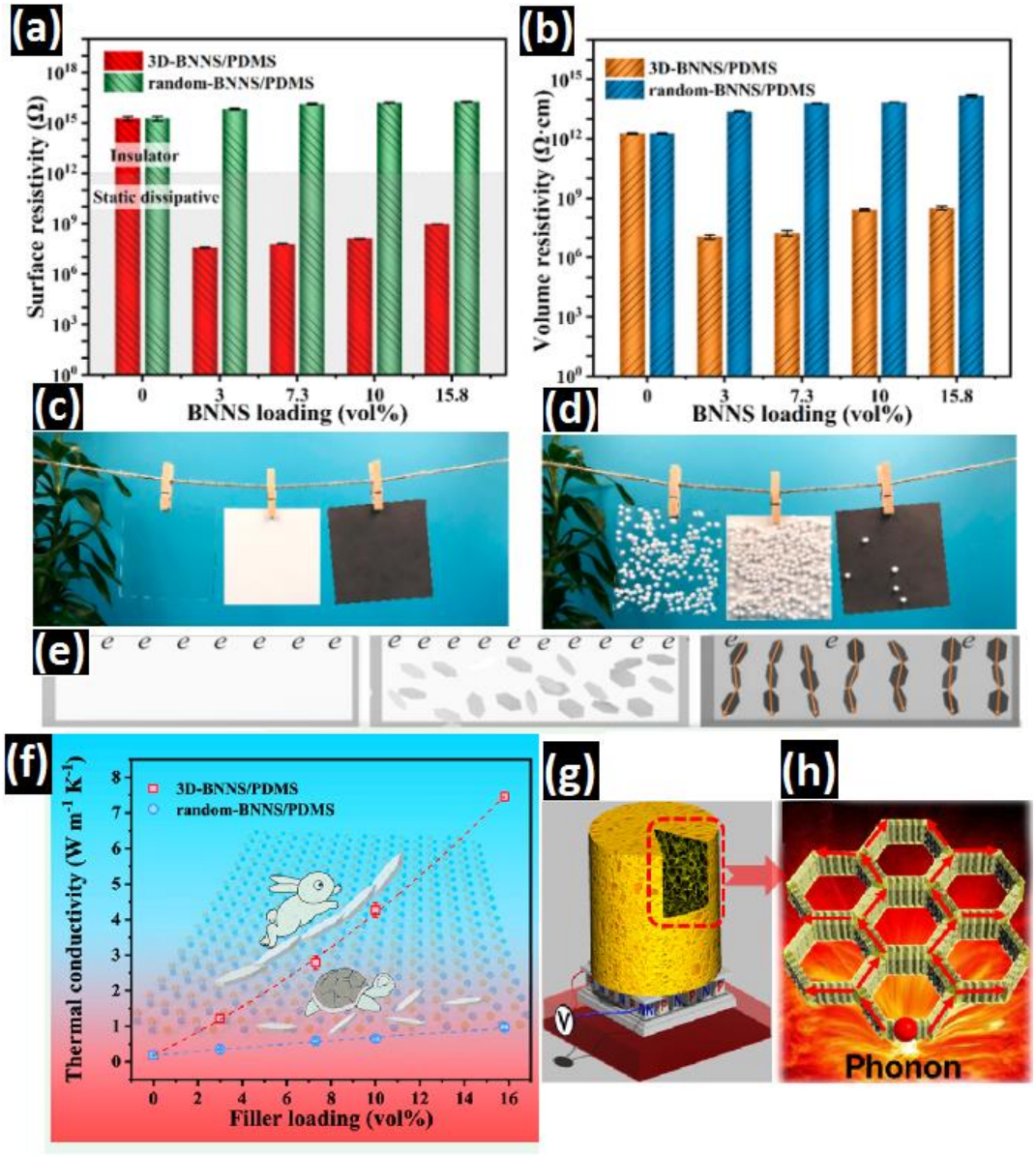

Figure 8. (**a**) Surface resistivity, (**b**) volume resistivity, digital image (**c**) before and (**d**) after electrostatic adsorption of polystyrene spheres, (**e**) schematic diagram of static dissipation of pure PDMS, random BNNSs/PDMS, and 3D-BNNSs/PDMS composites (sample size: 10 cm × 10 cm), (**f**) the comparison of TC value for two BNNSs/PDMS composites with different structure (Reprinted with permission from American Chemical Society, Copyrights 2019) [53]. Schematic illustration of (**g**) the Aerogel for thermoelectric generator device and (**h**) phonon scattering through the aerogel structure (Reprinted with permission from American Chemical Society, Copyrights 2019) [54].

Similarly, Functional BN/Polyimide (FBN/PI) aerogel was also fabricated using the freeze-drying, a light-weight and elastic thermal conductor composite. The particular cellular honeycomb structure of FBN-PI has given rise to the anisotropic TC with 6.70 and 2.20 W m^{-1}·k^{-1} for out-of-plane and in-plane directions at 30 °C, respectively. The schematic design of aerogel for thermoelectric generating purpose and phonon scattering through the structure are given in Figure 8g,h, respectively [54]. Xiao et al. [58] fabricated an epoxy resin-based composite having hollow h-BN microbeads (BNMBs). They utilized the salt-template technique to synthesize the hollow BNMBs and introduce the epoxy resin via the infiltrating method. The segregated structure of this composite with the optimized amount of 65.6 vol.% hollow BNMBs improved the TC of the neat polymer matrix from 0.2 W m^{-1}·k^{-1} to 17.61

and 5.08 W $m^{-1}{\cdot}k^{-1}$ for in-plane and out-of-plane directions, respectively. For determining the practical application of these materials, h-BN composites were situated on a heating plate with a point-heating source to record the heat dissipation performance by a thermal imaging camera. This evaluation demonstrated that heat distributes more effectively in the sample with a bigger size and higher vol.% of h-BN, without a concentration in one spot. The impact of different h-BN sizes in heat dissipation revealed that in sample A (composite with 10 µm h-BN and not as compressed as other samples), the approximative spherical-shape of h-BN microspheres brought a near isotropic low TC. Sample B, which is more compressed than sample A but with the same h-BN size, resulted in a drastic rise of TC in the out-of-plane direction. This behavior is due to the more compact thermal channels of the structure. Sample C represented h-BN 35 µm-V composite and possessed the adequate heat dissipation, owing to the orientated heat conductive pathways formed by large h-BN microspheres [58].

The BNNSs/epoxy resin composite (with 15 vol.% BNNSs) has also been fabricated through the freeze-drying method with the ultimate purpose of having a nacre-mimetic 3D thermally conductive network with strong thermal stability. As is reported, the achieved TC of 6.07 W $m^{-1}{\cdot}k^{-1}$ for BNNSs/epoxy can reach up to almost 32 times higher than the TC value of bare resin, showing the significance of h-BN. To substantiate the commercializing potential of this composite, Han et al. [52] had compared a commercial silicone sheet and BNNSs/epoxy composite as TIMs, which were integrated within a 20W LED chip and a Cu heat sink (Figure 9a,b). An Infrared camera tracked the changes in the surface temperature of the LED chips. Figure 9c presents the temperature change map for both chips in different time durations after lighting up the LED chips. It can be seen that the Silicone chip faces a sharp rise in temperature, comparing to BNNSs/epoxy composite. The impressive 10 °C difference in temperature change (Figure 9d) reveals the exceptional functionality of BNNSs/epoxy composite in heat dissipation applications. Plus, the thermal stability of this composite was investigated in Figure 9e by recording chip temperature in "on" (4 min) and "off" (2 min) stages, showing top-notch thermal stability [52].

Ball milling, high-pressure compression, and low-temperature sintering approaches have also been employed to obtain thermoset Polymer/h-BN composites. The Polyimide (PI)/h-BN composite reported by Wang et al. [60] was shown having a promising in-plane TC of 2.81 W $m^{-1}{\cdot}k^{-1}$ compared with pure PI (0.87 W $m^{-1}{\cdot}k^{-1}$) due to dense and adequate thermal pathways along this direction [60]. Although possessing both high TC and flame-retardancy behavior is challenging to reach, Tian and co-workers [61] reported an h-BN PMC with the mentioned performance. This composite had been fabricated via molding techniques with h-BN skeleton (sBN) (12.53 vol.%)/Phosphorus-free Bismaleimide (BD) resin, which exhibited a 1.53 W $m^{-1}{\cdot}k^{-1}$ TC and enhanced the bare BD resin performance 9.4 times along with releasing a fewer smoke amount (42.5%). The flame-retardancy examination of pure BD resin and BD/h-BN composites with different h-BN structures revealed that sBN/BD with its high TC transmits the generated heat faster than other samples through the material. This performance prevents the drastic temperature rise in the material and delays the degradation of the local material. Plus, the 3D porous framework structure of the sBN/BD composite improves the fabrication of a protection layer on the surface of BD resin. This structure enhances the development of a continuous carbon layer and the quality of char graphitization after combustion. On the contrary, the formed char on the BD resin surface was loose with visible micro-cracks and could not act as a useful protector. The BN/BD composite flame-retardancy performance is between the bare BN and sBN/BD, owing to its medium heat conductivity and deficient char protection layer [61]. Moreover, Silicon rubber has also been extensively utilized as a polymer substrate possessing outstanding TC, a wide range of temperature stability, and electrically insulation behavior. Further enhancement of silicon rubber can be done by adding 39.8 vol.% vertically aligned h-BN as filler via rolling technique, to form active thermally conductive paths through the polymeric matrix. This leads to achieving a 5.4 W $m^{-1}{\cdot}k^{-1}$ in TC, almost 33 times higher than the pure Silicone Rubber [63].

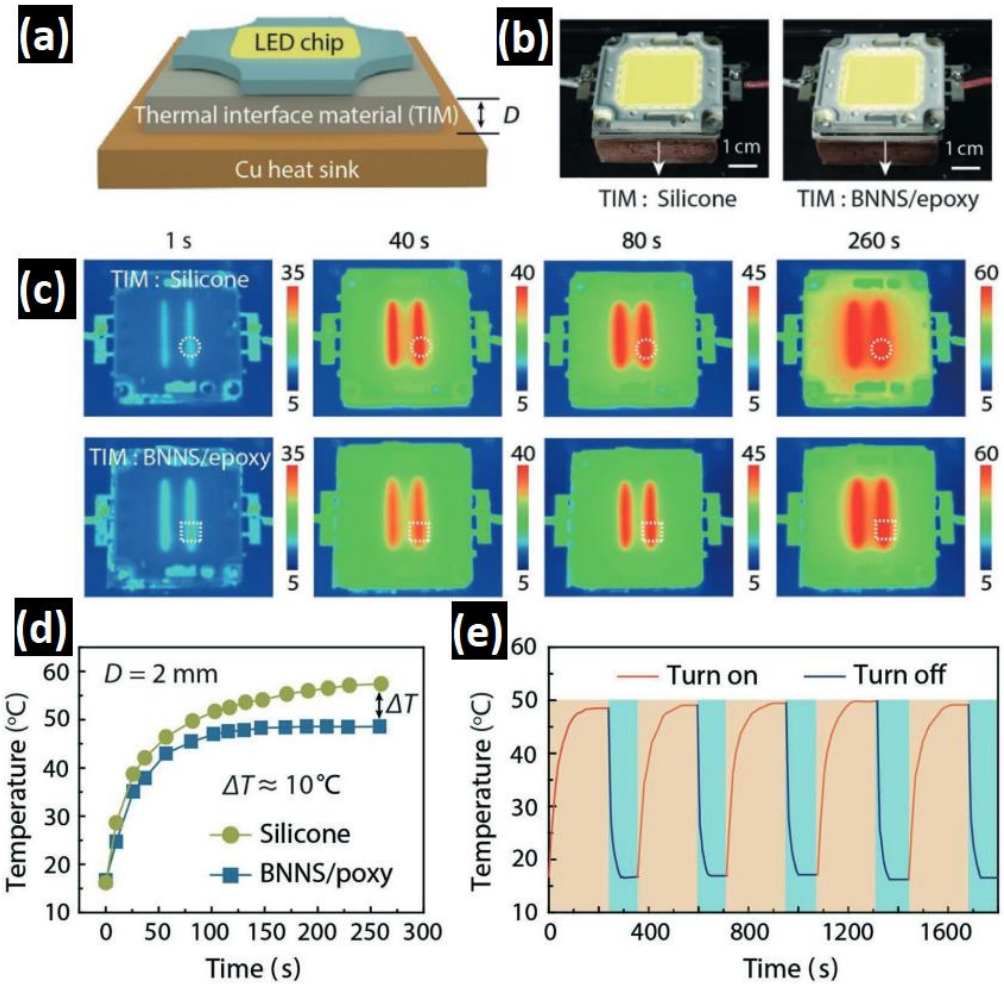

Figure 9. Demonstration of the as-mentioned BNNSs/epoxy composite as a TIM: (**a**) Schematic diagram of a light-emitting device (LED) chip integrated with a TIM and a Cu heat sink; (**b**) Optical images showing two LED chips integrated with commercial silicone and our BNNSs/epoxy composite as TIMs (both TIMs are 40 mm × 40 mm × 2 mm in size); (**c**) Sequential top-view infrared images of the two LED chips, indicating more efficient thermal dissipation using the present composite as TIM; (**d**) Comparison between the temperature increase of the same spot on the two chips, depicted by the white dotted circle and square, respectively, in (**c**); (**e**) The chip temperature monitored during cyclic "on" (4 min) and "off" (2 min) states, indicating the thermal stability of our BNNSs/epoxy composite (Reprinted with permission from WILEY-VCH, Copyrights 2019) [52].

2.4.2. h-BN within Hybrid Filler Configurations

Apart from polymers, hybrid fillers can potentially escalate the effectivity of the fillers' role throughout the matrix, more than individual h-BN sheets. The combination of different thermal conductive fillers like CNT [35,71], Graphene [72–74], Graphite [27,75], ZnO [76], Al_2O_3 [77], and so on, with h-BN, leads to a synergetic effect in the TC performances among counterparts [68]. As an example, a promising hybrid nanocomposite of in-situ grown CNT on BNNSs embedded in epoxy resin exhibited a 615% and 380% TC performance improvement for the cross-plane direction compared with pure epoxy and BNNSs/epoxy composite, respectively. Adding a low volume of CNT (2 vol.%) builds bridges between BNNSs and improves their connectivity. Plus, BNNSs blockage of CNTs path maintains the electrical resistivity of the hybrid composite [68]. Another appealing hybrid composite is the vertically self-aligned BNNSs (50 wt.%)–FeCo (30 wt.%) as fillers in poly (diallyldimethylammonium chloride) (PDDA) as the matrix. The unique structure of this composite shown in Figure 6c brings the thermal dissipation channels by transferring more phonons through a superior thermally conductive pathway

and increases the TC of PDDA from 0.11 to 2.25 W $m^{-1} \cdot k^{-1}$ [62]. Graphene can also be considered as a potential phonon-transferring substrate for h-BN. This is due to the relative resemblance of their thermal expansion coefficients (TEC), making a desirable behavior for high heat dissipation [78]. For instance, by taking advantage of the synergic effects of a self-assembly RGO/h-BN and introducing to the Silicone Thermal Grease (STG), Liang et al. [64] could improve the TC value up to 68% upon addition of 12 vol.% RGO/h-BN. Figure 10a,b reveals the proper heat dissipation performance of RGO/h-BN/STG compared to h-BN/STG and pure STG. Infrared thermal imaging was used to study the thermal management potential of RGO/h-BN/STG, h-BN/STG, and STG. Thermal map of heating and cooling steps (Figure 10a) demonstrates an accelerated and visible color change for RGO/h-BN/STG, indicting the most productive heat absorption from the hot-stage among other samples. The cooling curves of the samples are also plotted in Figure 10b. It is clear that the RGO/h-BN/STG presented the fastest cooling rate, followed by h-BN/STG and bare STG. This excellent behavior is raised from the higher TC and lower thermal resistance of this composite comparing with other samples [64].

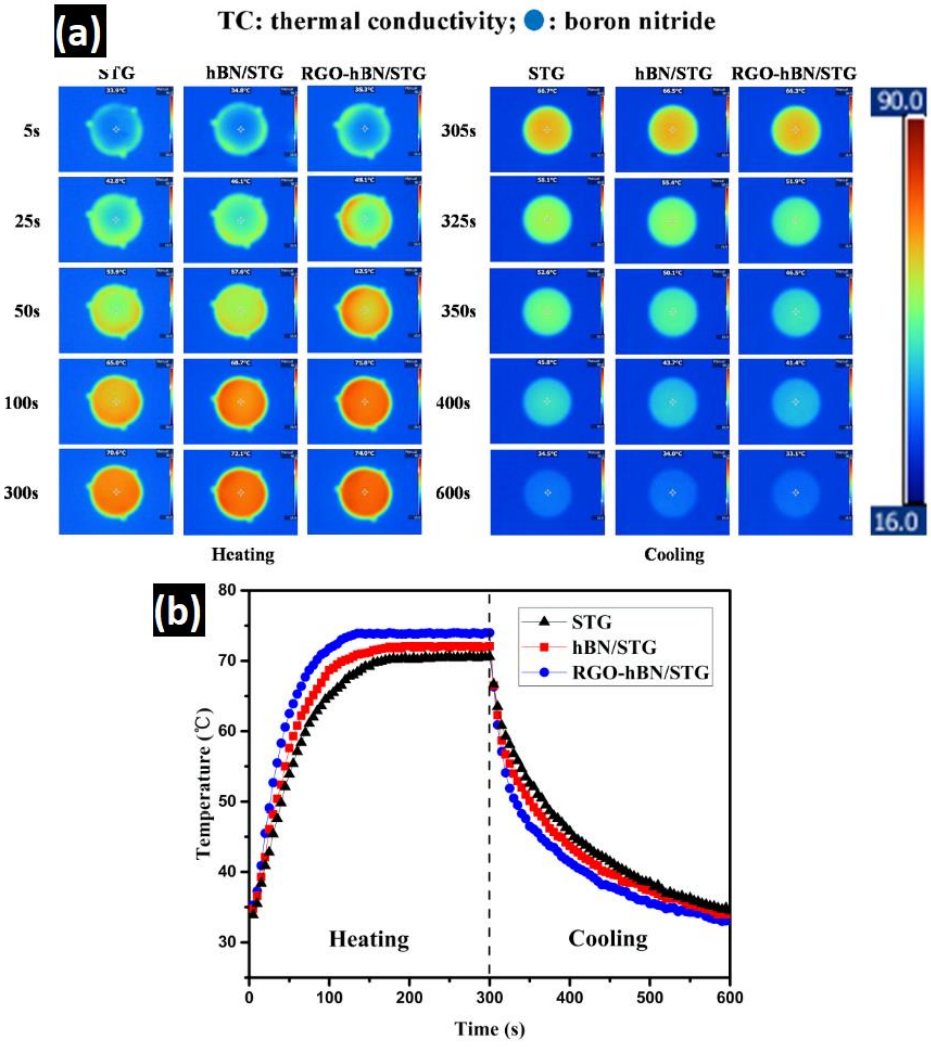

Figure 10. (**a**) Images recorded by a thermal imager with specimens heated on a homothermal platform and (**b**) the surface center temperature profiles of the samples as function of heating time (Reprinted with permission from MDPI, Copyrights 2019) [64].

Glass Fiber cloth (GF)/epoxy is one of the highly demanded functional composites in a wide range of applications such as aerospace, electronics, and electrical fields due to its superior chemical inertness and electrical resistivity [79]. However, these PMCs suffer from poor interfacial adhesion to the epoxy matrices causing a gradual degradation in the mechanical properties and lowering the TC [80].

These drawbacks which have limited GF/epoxy applications in the electronic industry, are shown to be solved by the addition of h-BN as a thermally conductive filler. Tang et al. reported a laminated hybrid GF/spherical h-BN/epoxy composite, made by blending-impregnation and hot compression. The as-fabricated composite exhibited considerable improvement in both vertical (3 times) and parallel directions (6 times) [81]. Table 1 summarizes the recent efforts devoted to the improvement of thermoset polymer matrices' TC.

Despite the high potential of thermoplastic polymer matrices, their integrations with h-BN fillers are much less explored compared with thermoset polymer matrices [12]. Polyethylene glycol (PEG) is one of these promising thermoplastic polymers with the feature of phase changing, making it capable of storing and releasing the thermal energy through a cycle. This potential suits them for many applications such as energy conversion, intelligent textile engineering, and heat management of different electronic parts [82,83]. Nevertheless, they exhibit deficient mechanical properties and low TC. As the earliest attempt, Yang et al. [84] addressed these challenges by encapsulating PEG with BNNSs-doped Cellulose nanofiber, resulting in a shape-stable PEG-composite and 42.8% improvement in TC upon addition of 1.9 vol.% BNNSs. Thermoplastic polyurethane (TPU) polymer matrices are other engaging polymer materials for miniaturized high-power electronic devices. One research in this area showed the significant role of BNNSs size (large and small) and volume content on the TC of TPU. The TC results showed that BNNSs (10 wt.%)/TPU composite reached 14.7 W $m^{-1}{\cdot}k^{-1}$ in TC for in-plane direction. The enhanced thermal performance from nearly 0.5 W $m^{-1}{\cdot}k^{-1}$ can be ascribed to the connection of small BNNSs to the neighbor large BNNSs, forming a continuous thermal path, and structural reinforcement. The effect of S-BNNSs content is investigated in Figure 11a. The higher S-BNNSs content (Up to 10 wt.%) results in the better TC, which is attributable to three reasons: First, the formation of heat conductive channels is developed by bonding S-BNNSs to their near L-BNNSs. Second, the S-BNNSs filled the gaps of L-BNNSs and constructed an interconnected structure through the matrix. Third, the S-BNNSs increased the filler-filler density, plotted in Figure 11b. The comparison of bare TPU and its nanocomposites is given in Figure 11c. It is visible that the 10 wt.% BNNSs/TPU is the optimized TPU nanocomposite in TC, which is originated from the advanced thermal channels built by the interconnection of S-BNNSs and L-BNNSs through the TPU network. A general comparison of the present nanocomposite with other TPU composite is presented in Figure 11d, showing the notable TC of this sample compared to others [59].

Table 1. Summary of recent PMCs reinforced with h-BN for enhancing thermal properties.

Matrix	Filler & Content	Procedure	Outcome	Other Features	Ref.
Epoxy	Hollow h-BN microbeads (65.6 vol.%)	Salt-template, Infiltration	17.61 W $m^{-1}{\cdot}k^{-1}$ (↑ 88 times)	Improved Thermal Stability, Lower Dielectric constant	[58]
Epoxy	BNNSs (15 vol.%)	Bidirectional Freeze-drying, Infiltration	6.07 W $m^{-1}{\cdot}k^{-1}$ (↑ 32 times)	Improved Thermal Stability	[52]
Epoxy	MWCNT (2 wt.%) – BNNSs (23 wt.%)	CVD, Exfoliation, Infiltration	~1.50 W $m^{-1}{\cdot}k^{-1}$ (↑ 6.15 times)	Enhanced Tensile Strength, Lower Dielectric constant	[68]
Epoxy	Expanded Graphite (2.5 wt.%)–h-BN platelets (70 wt.%)	Mixing, curing	2.08 W $m^{-1}{\cdot}k^{-1}$ (↑2.08 times)	-	[27]
Polyimide (PI)	Functional h-BN (50 wt.%)	Ball milling, freeze-drying, curing	9.8 W $m^{-1}{\cdot}k^{-1}$ (↑ ~32 times)	Hydrophobicity, Enhanced Thermal Stability	[54]

Table 1. *Cont.*

Matrix	Filler & Content	Procedure	Outcome	Other Features	Ref.
Polyimide (PI)	Functionalized h-BN (30 wt.%)	In situ polymerization, electrospinning, hot press	0.71 W m^{-1}·k^{-1} (↑ 4.73 times)	Enhanced Thermal Stability, Higher Glass Transition Temperature	[26]
Polyamide (PI)	h-BN platelets (20 wt.%)	Plasma-assisted mechanochemistry	3.68 W m^{-1}·k^{-1} (↑ 14.72 times)	Enhanced Young's Modulus	[85]
Phosphorus-free bimaleimide	h-BN skeleton (12.53 wt.%)	Frame molding, curing	1.53 W m^{-1}·k^{-1} (↑ 9.40 times)	Flame-retardancy	[61]
Silicone rubber	Vertically aligned h-BN (39.8 vol.%)	Rolling, curing	5.40 W m^{-1}·k^{-1} (↑ ~33 times)	Potential for TIMS	[63]
Silicon thermal grease (STG)	RGO–BNNS (12 wt.%)	Exfoliation, self-assembly, rolling	3.38 W m^{-1}·k^{-1} (↑ ~1.8 times)	-	[64]
Natural rubber	Functionalized h-BN platelets (30 vol.%)	Mixing, rolling	0.39 W m^{-1}·k^{-1} (↑ ~4 times)	Lower Dielectric Constant	[48]
Polydimethylsiloxane (PDMS)	BNNSs (15.8 vol.%)	Freeze-drying, carbonization	7.46 W m^{-1}·k^{-1} (↑ 39 times)	Antistatic Behavior	[53]
Polydimethylsiloxane (PDMS)	Graphite tube woven fabric (4.2 wt.%)–h-BN sheets (14 wt.%)	CVD, infiltration	3.10 W m^{-1}·k^{-1} (↑ 2.52 times)	-	[33]
Poly(m-phenylene isophthalamide) (PMIA)	Nano h-BN (30 wt.%)	Casting technique	0.94 W m^{-1}·k^{-1} (↑ ~4 times)	Low Dielectric Constant, Ideal Dielectric Loss	[47]
Poly(diallyldimethylammonium chloride) (PDDA)	BNNSs (50 wt.%)–FeCo nanocubes (30 wt.%)	Exfoliation, self-assembly, mixing	2.25 W m^{-1}·k^{-1} (↑ ~20.5 times)	Superb Flexibility	[62]
Thermoplastic polyurethane (TPU)	BNNSs (10 wt.%)	Ultrasonic exfoliation, self-assembly	14.7 W m^{-1}·k^{-1} (↑ 29.4 times)	-	[59]
Polyethylene glycol (PEG)	BNNS (1.9 vol.%)–doped cellulose nanofiber (2.5 wt.%)	Freeze-drying, layer-by-layer assembly, vacuum impregnation	0.40 W m^{-1}·k^{-1} (↑ ~0.5 times)	Excellent Shape Stability against Pressure, Tension, and Bending	[84]

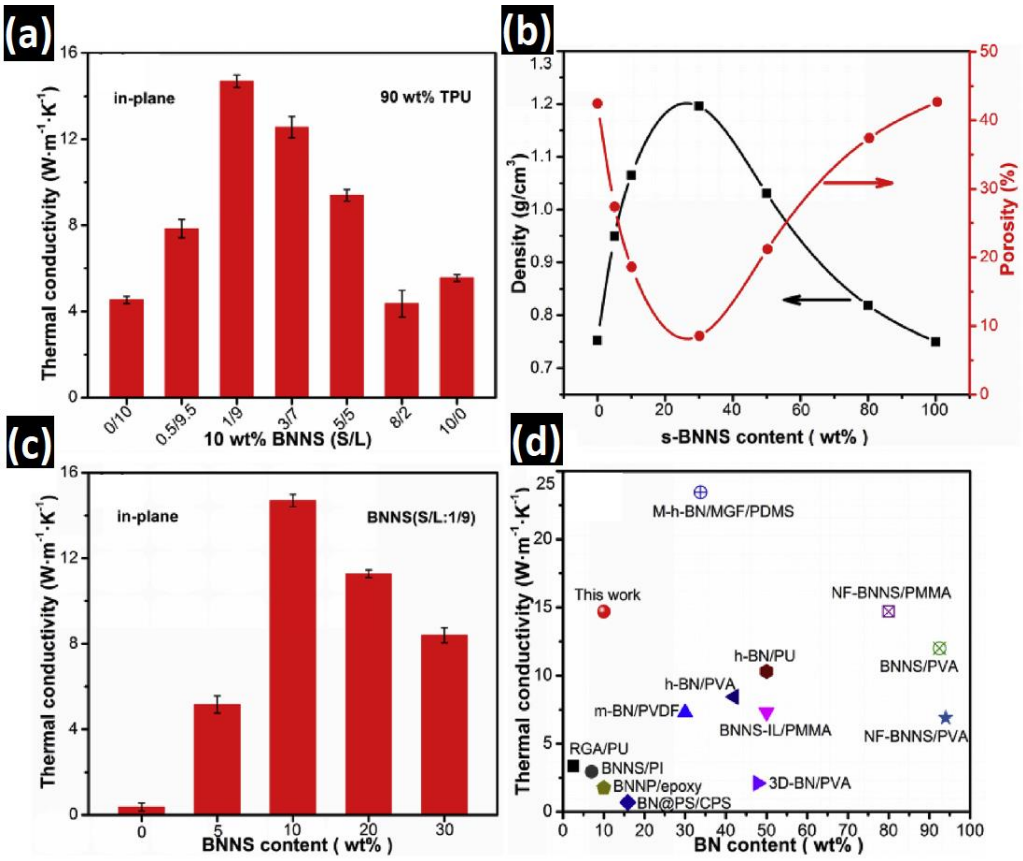

Figure 11. The S/L-BNNSs/TPU films with different S-BNNSs contents: (**a**) the in-plane TC, (**b**) density and porosity; (**c**) in-plane TC of the BNNSs/TPU films with different BNNSs contents; (**d**) comparison of the in-plane TC with h-BN fillers or TPU polymeric composites reported in previous studies (Reprinted with permission from Elsevier, Copyrights 2019) [59].

3. Tribological Properties

3.1. Tribology Theory

Historically, the study of tribology goes back to hundreds of years ago. In fact, the term of tribology is derived from the Greek word tribos meaning 'rubbing' [86]). However, the definition and science behind that are relatively new [87].

Generally, science of tribology studies the phenomena that is taking place between two moving surfaces [88] and it focuses on science of friction, lubrication, and wear involved in moving contacts [86,89]. Structural deformation, dimensional variations and degradation of sliding parts in commercial working systems necessitate the reduction of the friction and enhancing the performance of the involved counterparts [90]. Therefore, all aspects of mechanical, chemical, and materials sciences are involved simultaneously to boost up the performance of a system [86,91,92]. The earliest spikes of considering tribology as a science was seen in the development of high velocity internal combustion engines in the beginning of 20th century [93]. In fact, reduction of the friction and wear can mitigate energy consumption of the system. It also provide the appropriate condition for the fast and precise motions with minimum required maintenance cost and increment of the efficiency [94–100]. Having said that, tribology has rendered several valuable applications such as gas turbine engines, automotive parts, artificial human joints, hard disk drives for data storage and an increasing number of electromechanical devices [101–104].

3.1.1. Friction

Friction is the force resisting the sliding of two surfaces against each other and can be simply calculated by the Amonton's law [105]:

$$F = \mu W \quad (5)$$

where F is friction force (N), μ is coefficient friction (COF) (dimensionless), and W is normal load (N). From the tribological point of view, μ is an important factor determining wear rate of the components. Except the nature of the materials, COF mostly depends on the characteristics of the surface as well as lubrication condition [106–109]. Therefore, tailoring the surface characteristics and lubrication condition may optimize the performance of the components under friction [110–112].

3.1.2. Wear

Wear is the damage to a solid surface, generally involving progressive loss of material due to relative motion between the surface and a contacting substance or substances [87]. Despite the massive development in characterization equipment, it is still not possible to comprehend and examine the wear phenomena thoroughly. Hence, three main complexities can make the surface analyses difficult: (1) continuous alteration of the chemical composition on the surface within the process due to wear, (2) the changing surface topography of the specimen, and (3) the existence of complex and blended mechanisms of the wear [113–115]. Nonetheless, one common method of measuring the amount of wear is through the Archard wear equation, represented in Equation (6) [86,87]:

$$Q = KW/H \quad (6)$$

where Q is the volume removed from the surface per unit sliding distance, K is wear coefficient (dimensionless), W is the normal load applied to the surface by its counterbody, and H is the indentation hardness of the wearing surface. By variation of K, the severity of different wear processes can be compared. For instance, for a lubricated condition, it stands in the range of 10^{-14}–10^{-6} while a dry sliding process and usage of hard particles give the ranges of 10^{-6}–10^{-2} and 10^{-4}–10^{-1}, respectively (Figure 12) [86,87].

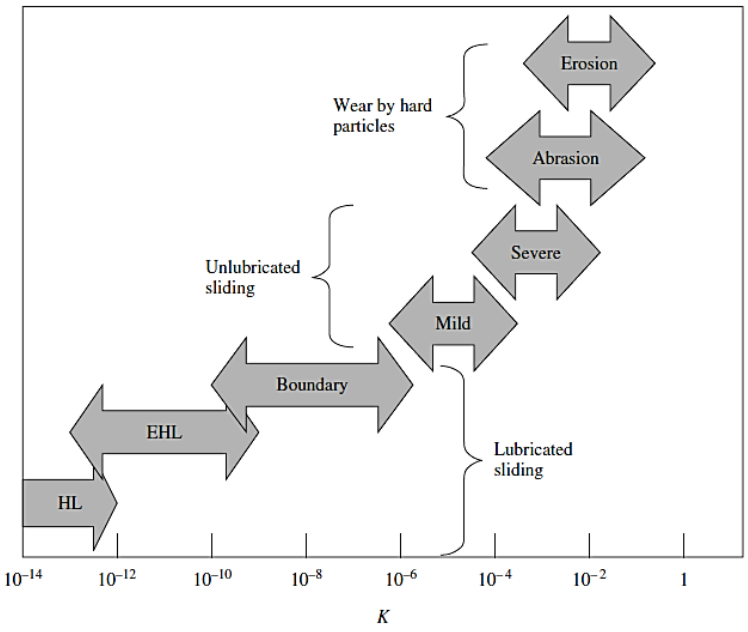

Figure 12. Schematic representation of the range of wear coefficient exhibited under different conditions of wear (HL: hydrodynamic lubrication; EHL: elastohydrodynamic lubrication) (Reprinted with permission from John Wiley & Sons, Copyrights 2005) [87].

3.1.3. Lubrication

Nowadays, production of hundreds of million lubricants' barrels per day indicates the indispensable roles lubrication in many industries [86]. In fact, performance and lifetime of the components struggling with friction and wear will be diminished without employing lubricants. As can be seen in Figure 12, a low amount of lubricant (falls on the boundary lubrication) reduces the K by several orders of magnitude. The friction-lubrication relationship often is described by Stribeck diagram (Figure 13), in which COF (μ) is directly correlated to the viscosity of the lubricant (η) and difference in velocity of two sliding surfaces (V), while is inversely proportional to the normal load (P) (bearing number = ηV/P) [116–118]. When bearing number is high, μ linearly ascends and the mechanism is fluid film lubrication [116,117]. Indeed, by increasing the load or lubricant viscosity and/or decreasing the sliding speed, the bearing number gradually decreases. Thereafter, the lubricant film gets thinner, and consequently, COF declines to its minimum value [116,117]. For smaller bearing number values, the reducing trend of lubricant thickness continues, and the asperities of the rubbing surfaces interact slightly, causing an increment in the COF. This behavior is known as mixed lubrication mechanism [116,117]. Further declination of the bearing factor causes more severe interaction of the sliding surfaces attributing to thinner lubricant and higher COF value. This regime is often characterized by boundary lubrication [116,117].

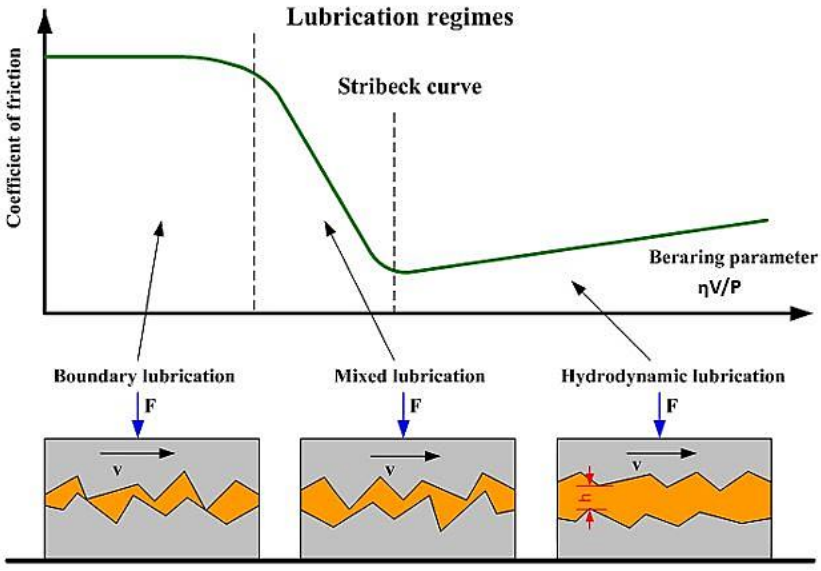

Figure 13. A Stribeck curve and illustrations of the lubrication regimes (Reprinted with permission from Nature, Copyrights 2016) [118].

3.1.4. Solid Lubrication

Solid state lubricants compounds are famous for decreasing COF and increasing wear resistance of sliding parts [28,119]. Their high stability can suite them for harsh conditions that liquid lubricants cannot tolerate. Stable functionality at elevated temperature (>350 °C), ultra-low temperatures (e.g., liquid nitrogen working temperature) or under ultrahigh load, severe oxidation, ultrahigh vacuum, and intense radiation are a few examples of their merits [120–122]. In addition, they can be used in form of free-flowing powders, anti-friction pastes, anti-friction coatings, and oil additive [122]. Solid lubricant compounds, by providing boundary lubrication, help the COF and wear reduce. One vital element to consider is the thin layer that is transferred from the surface of lubricated surface to the counterface, named tribo-film, tribo-layer, or transfer film [123–125]. Moreover, there are a broad variety of solid lubricants, e.g., inorganic materials with lamellar structure (graphite, h-BN, sulfides, selenides, tellurides, etc.), soft metals (Pb, Sn, Bi, In, Cd, and Ag), organic compounds with chain structure of the polymeric molecules (PTFE and polychlorofluoroethylene) [122]. Apart from

having the lamellar structure, h-BN is in the center of attentions due to capability of maintaining the lubrication characteristic up to 1200 °C in oxidizing environment [28]. Here we aim to survey the recent efforts devoted to composite manufacturing by h-BN as a lubricant with the perspective of tribological studies.

3.1.5. Materials Development

PMC

Growing needs to light-weight materials possessing self-lubricating characteristics as well as high chemical stability in aqueous solution has urged researchers to manufacture new PMCs suitable for aqueous media applications such as ships, water pumps, and washing machines [126–128]. However, by working under a high loading and low-velocity condition, the created water film does not reveal a high carrying capacity because of the low viscosity which results in a mixed or boundary lubrication condition [129]. Hence, fabrication of durable tribo-materials for aqueous media lubrication condition is highly demanded. Considering that wear for wet friction is considerably lower than any dry friction (due to prevention of water medium from material transfer and tribo-chemical phenomenon and lowering the interface's temperature), addition of reinforcements will lead to the generation of a lubricating film [130]. In this regard, h-BN has represented supreme lubrication behavior in water medium [131,132]. For instance, COF of h-BN/h-BN rubbing pair in aqua is reported 0.06–0.12, while it is 0.18–0.25 in dry friction [133,134]. The reason behind this low COF in water lubrication condition is claimed the reaction of h-BN with water molecules, resulting in the formation of a tribo-chemical layer consisting of H_3BO_3 and B_2O_3 [29,135]. However, regarding the self-lubricating performance of the tribo-chemical layer, it is declared that H_3BO_3 plays the leading role owing to its layered triclinic structure [136]. Taking advantage of the self-lubrication characteristic and low liquid absorption ratio of polyformaldehyde (POM), Gao et al. [137] constructed POM/3 vol.% h-BN composite and studied its tribological behavior in the water medium. Assessments revealed that the COFs of both POM and POM/h-BN have reduced gradually by increasing the sliding time, while the composite represented lower COF, especially when the applied load was increased from 50 N to 200 and 300 N. In parallel, the addition of h-BN reduced the wear rate significantly. For instance, in low and high loads, the wear rate was about one order of magnitude lower than neat POM. The obtained attenuated total reflectance Fourier transform infrared spectroscopy (ATR-FTIR) spectra of the inside and outside of the wear scar indicated no sign of adsorbed water (Figure 14a,b), meaning the composite is suitable for utilizing in aqueous environment. More importantly, an excess band at 945 cm^{-1} appeared on the worn surface, attributing to H_3BO_3 (Figure 14a), which is responsible for the superior lubrication performance of the h-BN composites. The below equations can describe how this surviving compound has been formed,

$$2BN + 3H_2O \rightarrow B_2O_3 + 2NH_3 \quad (7)$$

$$B_2O_3 + 3H_2O \rightarrow 2H_3BO_3 \quad (8)$$

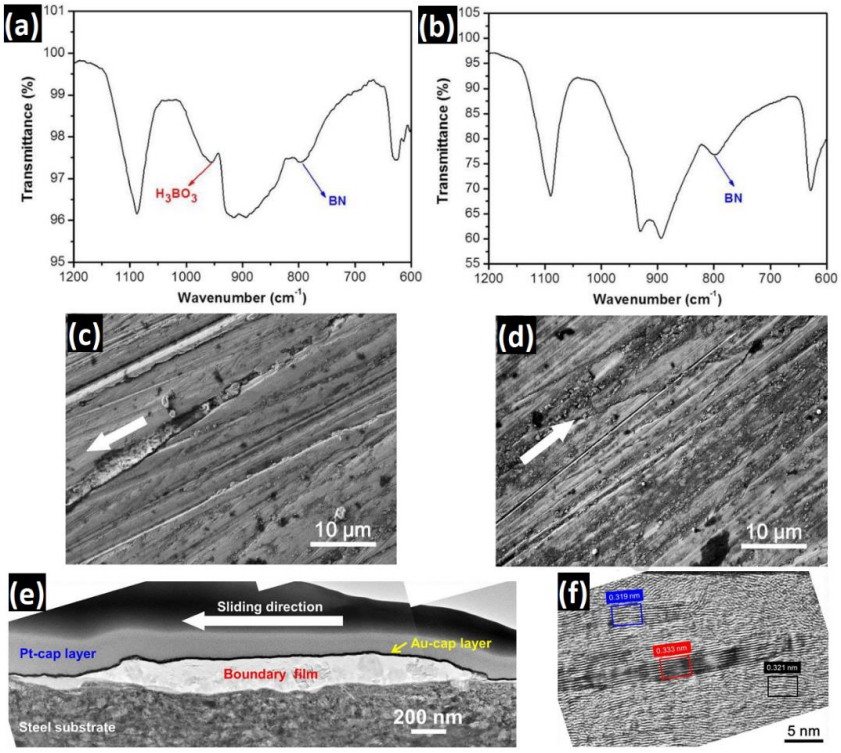

Figure 14. ATR-FTIR spectra of surface areas within (**a**) and outside (**b**) of the wear scar of POM/3hBN at applied load of 200 N; SEM graphs of the steel counterface after rubbing with (**c**) neat POM and (**d**) POM/3h-BN at applied load of 200 N (Arrows indicate the sliding directions); (**e**) overview of the TEM graph of focused ion-beam cut cross-section of the boundary film formed on steel surface after sliding against POM/3hBN at 200 N; (**f**) high resolution TEM (HR-TEM) graph of the outmost layer of the boundary film (Reprinted with permission from Elsevier, Copyrights 2017) [137].

Moreover, the SEM images taken from the steel counterface after rubbing with POM and POM/h-BN illustrated that the detached particles of POM are concentrated into the roughness trenches, but the flat areas are mostly intact (Figure 14c). While in the composite rubbing case, the boundary film is spread over the whole steel counterface (Figure 14d), resulting in higher wear resistance of POM/h-BN. Figure 14e, depicts the transmission electron microscopy (TEM) image of the continuous boundary film formed on the steel after rubbing with POM/h-BN. The energy dispersive X-ray (EDX) analysis showed the top layer of the boundary film is a B-rich layer, and the measured lattice fringes of 0.319 and 0.321 nm proved the existence of H_3BO_3 and B_2O_3, respectively (Figure 14f (refer to the tribo-chemical reactions of Equations (7) and (8))). Also, there exist some intact h-BN with 0.333 nm lattice fringe. Having considered that, these layers are oriented in parallel to the sliding direction, which enhance the lubrication capability. Moreover, it is shown that using only 10 vol.% carbon fiber (POM/10CF-3hBN) reduces the wear rate by about 50%, which is originated from reinforcing synergic effect of the fiber and boundary layer of h-BN [137].

Epoxy is a popular polymer for structural applications; however, it has a serious shortcoming, i.e., low wear resistance due to forming a 3D cross linking network during the curing process [138,139]. Adding nano-fillers is a promising way to compensate the poor tribological performance of epoxy. For example, -OH functionalized h-BN and c-BN were utilized to improve tribological properties of epoxy coating [140]. Observations showed that there were some long cracks in the neat epoxy coating, while BN nanofillers acted like a barrier against cracks and hindered their expansion. The outcomes of the COF evaluation indicated that the minimum value belongs to composites containing 0.5 wt.% h-BN and c-BN, with 12.4 and 9.74% lower COF in comparison to neat epoxy in dry rubbing test, as well as 39.27 and 30.03% lower COF in comparison to neat epoxy in seawater sliding condition, respectively. Except increasing the toughness of the composite through hindering propagation of

cracks, forming a solid boundary film caused reduction of the COF of the composites. Wear rate results showed significant improvement for both reinforcements; however, c-BN reinforced composite was a little better. For example, the wear rate of epoxy/h-BN reduced 73.61 and 68.36% with respect to pure epoxy under the dry and wet sliding condition, respectively. Remarkable performance of the composite in seawater condition is attributed to diminishing the direct contact of the sliding surfaces which declines adhesive wear, taking away the generated frictional heat which prevents thermal softening, removing the produced wear debris which results in smoother and cleaner surface [140]. In a similar work, polydopamine (PDA) was used to functionalize the BN nanofillers in order to better dispersion within the epoxy matrix; moreover, the binary reinforcements containing both h-BN and c-BN with proportion of 1:2 (HC12), 1:1 (HC11), and 2:1 (HC21) were examined [141]. As can be seen in the cross-section profiles of the depth of wear cracks (Figure 15a), in dry condition the maximum value belongs to pure epoxy with 46 μm and the minimum values belong to HC21 and c-BN with 14 and 12 μm, respectively. Under wet sliding test, the results were different; pure epoxy revealed a depth of 68 μm which was the maximum for sure, and for HC21, HC12, and c-BN its was 2.7, 3.6, and 1.3 μm, respectively (Figure 15c). The wear rate was more or less following this sequence which is illustrated in Figure 15b,d. Obviously, c-BN represented better results than h-BN due to its higher hardness. However, when the reinforcement was contained both of them, the composite showed excellent anti-wear behavior due to synergy of hard cubic phase of BN and good lubricity of hexagonal phase of BN [141].

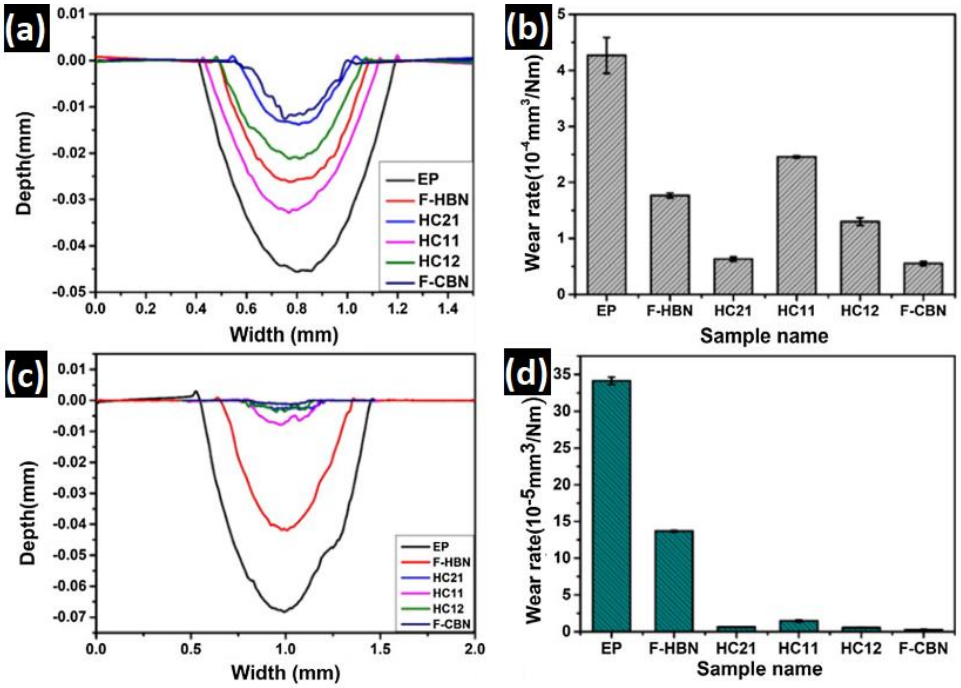

Figure 15. Cross-section profiles of the h-BN@PDA/c-BN@PDA/epoxy coatings (**a**) under dry sliding, and (**c**) seawater condition; wear rate of the h-BN@PDA/c-BN@PDA/epoxy coatings in (**b**) dry sliding, and (**d**) seawater condition (Reprinted with permission from Elsevier, Copyrights 2019) [141].

Poly aryl ether ketone (PAEK) is the other polymer which has a great potential to be used in tribological applications [142]. In a new study, the effect of adding micro and nano h-BN as secondary solid lubricant was studied [143]. In this regard, the composite of PAEK/30glass fiber-10graphite-10h-BN (named C_{HM}) was chosen as the baseline, and then 3% of h-BN was substituted by nano h-BN (named C_{HN}). Evaluations revealed that by adding nano h-BN the value of COF and wear rate diminished at both low and high sliding velocity. According to Figure 16a,b, the boundary film in C_{HM} is thick and discontinuous, while that of C_{HN} is smooth and uniform. Besides, SEM images of the worn surfaces indicate that the

fibers in C_{HM} are cracked and debonded (Figure 16c,d), resulting in high wear. The labeled area in Figure 16c, show (1) debonding of large fibers, (2) broken and disoriented fiber pieces causing high friction, (3) an array of fiber pieces that have just been broken and are about to become disoriented on further shearing, (4) cavities left after removal of fibers and materials. In contrast, there is not much evidence of cracking or debonding of the fibers in the case of C_{HN} [143].

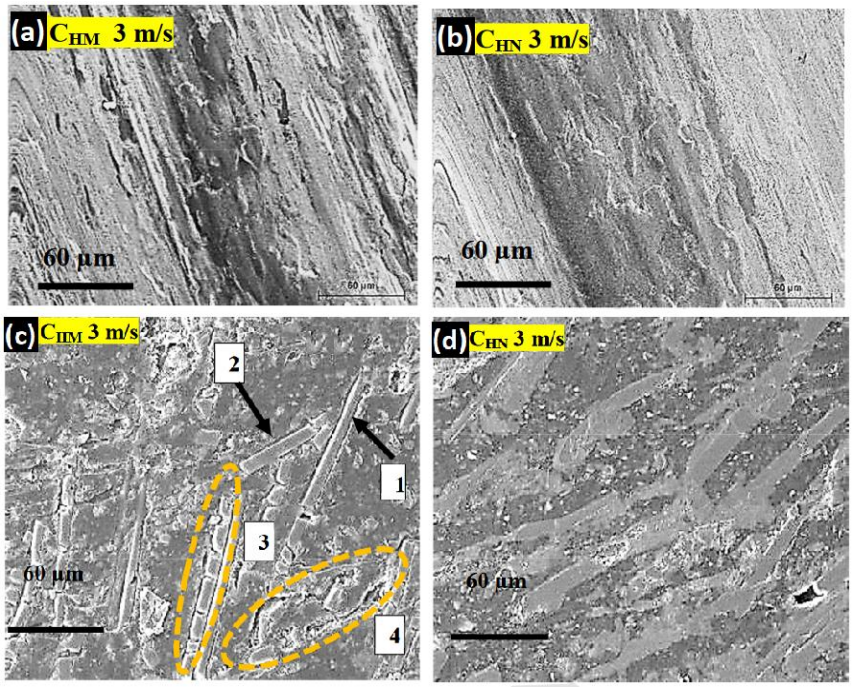

Figure 16. SEM images of (**a**,**b**) worn disc surfaces of C_{HM} and C_{HN} under 900 N and 3 m s^{-1}; (**c**,**d**) worn pin surfaces of C_{HM} and C_{HN} (Reprinted with permission from Elsevier, Copyrights 2019) [143].

Ceramic Matrix Composite (CMC):

Typically, fiber reinforced CMCs represent the best mechanical performances among different kind of them. One important strengthening mechanism in this group of composite materials is crack deflection in which lubricity between the fiber and matrix seems essential [144]. Conventional solid lubricants for SiC fiber are pyrolytic carbon and h-BN [145]. The main advantage of h-BN coating is the ability of working in high temperature oxidizing environments [146]. However, this process is challenging since depositing a uniform crack free layer on fibers is difficult. Recently, a uniform layer of h-BN was successfully substituted graphene oxide (GO) on SiC fiber by Tak et al. [147] In this process, utilizing (3-amonipropyl)triethoxysilane the surface of SiC fiber was modified with amine groups. Therefore, GO deposited on the fiber and by heating at 1200–1400 °C under N_2 and NH_3 atmosphere. By increasing the temperature from 1200 to 1400 °C, the thickness of the coating increased from 10 nm to 1.10 µm (Figure 17a–c). However, in order to obtain a high crystalline structure heating at 1400 °C is necessary.

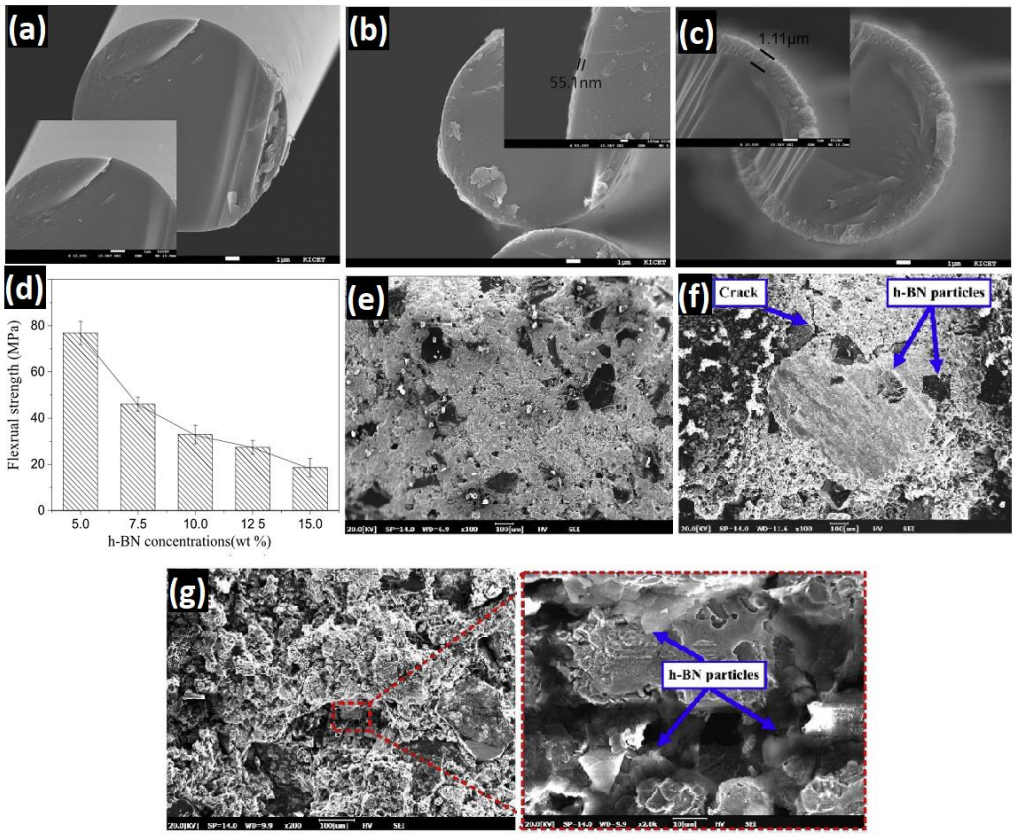

Figure 17. Morphology of fiber at reaction temperatures of graphene oxide to boron nitride: (**a**) 1200 °C, (**b**) 1300 °C and (**c**) 1400 °C (Reprinted with permission from Springer, Copyrights 2020) [144] (**d**) Friction coefficient versus h-BN concentrations; SEM images of the worn surface of composites after testing with different h-BN amount, namely, (**e**) 5, (**f**) 10 and (**g**) 15 wt.% (Reprinted with permission from Elsevier, Copyrights 2020) [148].

Two thermodynamically stables allotropes of BN (h-BN and c-BN) have also been utilized as reinforcement and matrix, respectively [148]. It's been shown that addition of h-BN flakes as lubricant to the self-lubricating c-BN composite improves the wear behavior of as-prepared composites, although negatively affects fracture strength. c-BN prepared via powder metallurgy, Cu-Sn alloy powder and Ti particles mixed with different amounts of h-BN from 5 to 15 wt.% were used to make the specimens which were tested in a ball on disc setting. Considerable reduction in COF from 0.7 to 0.21 has also been observed by increasing the h-BN from 5 wt.% to 15 wt.%, proving the role of h-BN in wear characteristic enhancement of the composites. Figure 17d shows the COF in five different amount of h-BN 5 wt.%, 7.5 wt.%, 10 wt.%, 12.5 wt.% and 15 wt.%. As it is obviously observable in the diagram, the major drop is shown in increasing h-BN from 10 wt.% up to 12.5 wt.% which is from 0.58 to about 0.35 [148]. To interpret the fracture mode transformation of the composite through increment of the h-BN content, SEM micrographs of the ball's worn surface as a function of the h-BN concentration are shown in Figure 17e–g. As can be seen, by increasing the h-BN from 5 wt.% to 15 wt.%, the fracture mode has transformed from trans-granular into inter-granular. As can be seen, 5 wt.% of h-BN additive provides a relatively uniform dispersion of particles in the matrix (Figure 17e). However, increasing h-BN content to 10 wt.% leads to formation of micro-cracks in c-BN grains (Figure 17f). Therefore, with higher h-BN amount (up to 15 wt.%), the larger number of micro-cracks as well as micro-pores will appear (Figure 17g), resulting in lower mechanical strength. 10 w.t% h-BN represented the optimal tribological and mechanical properties [148].

A study on wear characteristics of Si_3N_4/h-BN ceramic composites under the marine atmospheric environment reflected a notable enhance in the tribological behavior of silicon nitride with the addition of the second phase of h-BN [149]. Adding 20 wt.% h-BN lowered the COF to 0.302, and the wear rate to 2.93×10^{-6} m^3 N^{-1} m^{-1} [150]. Figure 18a,b show the worn surface of Si_3N_4 and Si_3N_4/20% h-BN, respectively, and the smoother worn surface in 20% h-BN is obvious. This improvement is the consequence of forming a tribo-chemical film on a worn surface. In marine atmosphere, plenty of ions will encourage the formation of a tribo-chemical film and higher content of h-BN which rises up the viscosity of the tribo-chemical film, will increase the resistance of the film [150].

h-BN is also used to boost the tribological properties of carbon nanotubes (CNTs). In a research by Yuan et al., composites of BNNSs produced by heating boric acid in a pure N_2 atmosphere and CNT in three different ratios (h-$BN_{0.75}C_{0.25}$, h-$BN_{0.5}C_{0.5}$, and h-$BN_{0.25}C_{0.75}$) were sintered for 48 h and finally sintered for 2 h at 180 °C [151]. The results of wear test of these samples are reflected in Figure 18c,d. It is shown that the composites with both h-BN and CNT tend to a reduction in COF as well as wear rate compared to CNT (COF = 0.1 and wear rate = 1.9×10^{-14} m^3 N^{-1} m^{-1} and h-BN (COF = 0.095 and wear rate = 2.2×10^{-14} m^3 N^{-1} m^{-1}). It is shown that the lowest COF is 0.075 and the lowest wear rate is 1.2×10^{-14} m^3 N^{-1} m^{-1} which belongs to h-$BN_{0.5}C_{0.5}$.

Metal Matrix Composite (MMC):

Apart from PMCs and CMCs, MMCs can also be reinforced by h-BN to enhance the tribological functionality. Among the alternatives, Cu, Al, Ni, and Fe have recently grabbed the consideration of tribology scientists. Owing to the supreme electrical and thermal conductivities of Cu, they are introduced as a platform of various industries; however, their applications are often suppressed by their low mechanical strength and wear resistance [152,153]. Hence, ceramic nanoparticles are often used to strengthen the Cu-matrix without considerable negative effect on the electrical and thermal conductivities [154]. One possible choice, in this group of reinforcements is h-BN, however, there is only one published report available. It was demonstrated that the addition of h-BN to the Cu matrix improves the lubricity of the final composite [155]. By detail, addition of 2.5 wt.% h-BN caused only 0.008 reduction in COF, while 5, 7.5, and 10 wt.% h-BN resulted in 0.079, 0.102, and 0.112 reduction, respectively (Figure 18e). That minor improvement for Cu/2.5 wt.% h-BN nanocomposite could be due to the pinning and alignment of h-BN planes by the matrix grains within the sintering process. Also, it seems the optimal amount is obtained by 5 wt.% h-BN since no further improvement was observed with higher h-BN contents (that could be due to random orientation of h-BN platelets). Moreover, as it is demonstrated in Figure 18f, wear rate increases by addition of h-BN relating to existence of low shear strength along the direction of rubbing [155].

Wear behavior of aluminum alloy (AA6082) reinforced by TiB_2 and h-BN nano particles has been investigated by Palanivel et al. [156]. In this research, the friction stir processing (FSP) was used as synthesis process. The shape and morphology of the nanosized h-BN particles were found unchanged during FSP, while fragmentation of TiB_2 particles varied during the process. Additionally, nano h-BN particles could enhance the wear resistance by formation of a tribo-film. Initially, the wear rate of the AA6082 itself was measured 23.75×10^{-5} mm^3 N^{-1} m^{-1}. However, by addition of TiB_2 and h-BN reinforcements, wear rate reduced around 35% and 40%, respectively. That's why AA6082/(TiB_2 + h-BN) hybrid composite showed the wear rate as low as 13×10^{-5} mm^3 N^{-1} m^{-1}. To understand the morphological difference of the samples, Figure 19a–d exhibit the SEM images of the worn surface related to pure AA6082, AA6082 composite containing TiB_2, TiB_2 + h-BN, and h-BN particles, respectively. As can be seen, Figure 19a indicates a plastic deformation happened in the parent material, and the worn surface of the composite reinforced by TiB_2 is covered by wear debris (demonstrated in Figure 19b). However, in Figure 19c, the worn surface is debris-free due to the lubricative role of h-BN as well as load distribution of TiB_2 to lower the material removal. In the other words, by acting as a solid lubricant, h-BN forms a tribo-film on the worn surface and creates a smoother surface [157]. Hence, it is expected that the presence of wear debris shown in

Figure 19b is due to the absence of h-BN. Lastly, wear debris in Figure 19d which are related to AA6082 and AA6082/h-BN particles is originated from material removal in the adhesive mechanism, which was much lower in the presence of TiB_2, as well as the abrasive mechanism [158]. Importantly, presence of TiB_2 and h-BN in the wear interface can altered the wear mechanism from adhesive to abrasive [156].

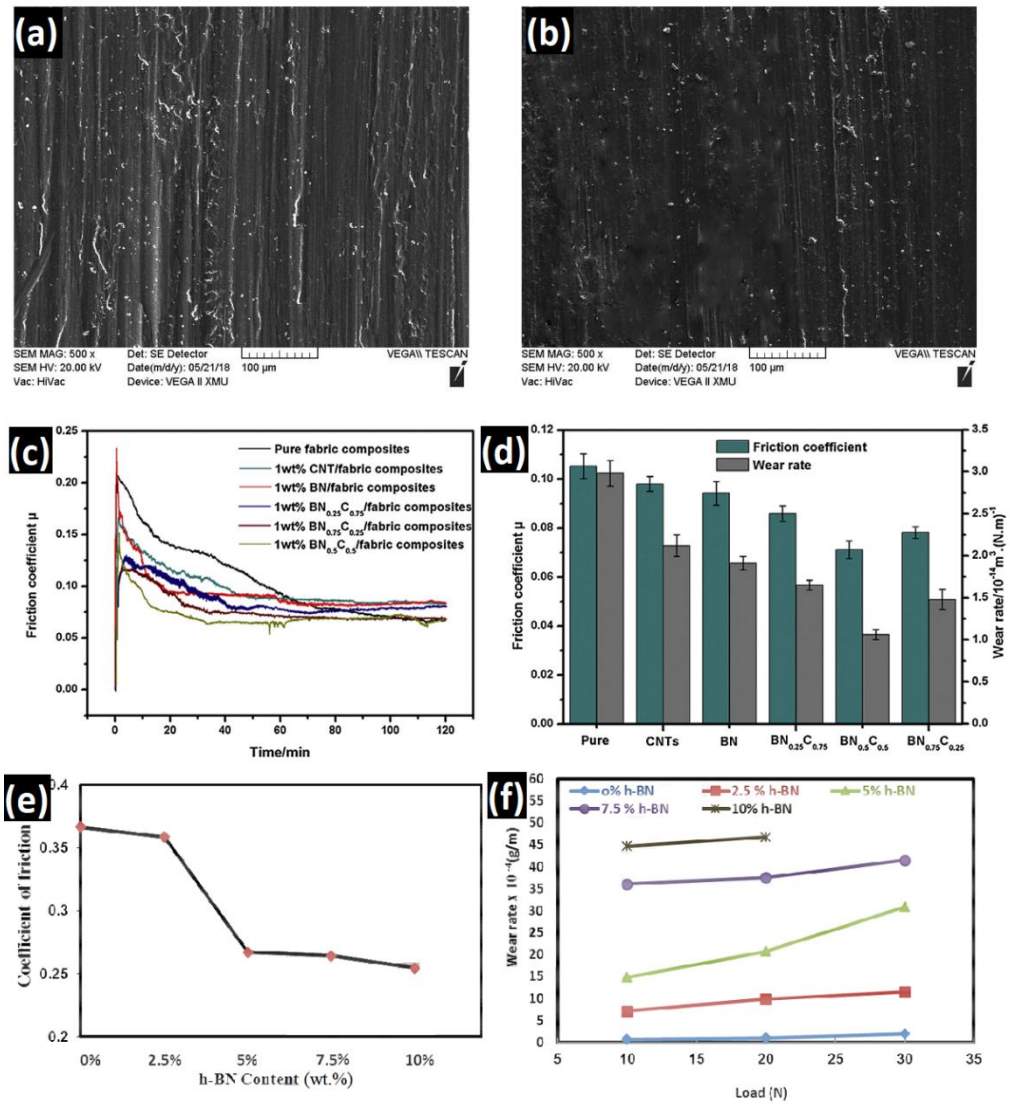

Figure 18. SEM micrographs of the worn surfaces of (**a**) Si_3N_4 and (**b**) Si_3N_4/20% h-BN (Reprinted with permission from Elsevier, Copyrights 2017) [150]. (**c**,**d**) Friction coefficient of pure composite and with CNT, h-BN, h-$BN_{0.75}C_{0.25}$, h-$BN_{0.5}C_{0.5}$, h-$BN_{0.25}C_{0.75}$ (Reprinted with permission from Elsevier, Copyrights 2019) [151]. (**e**) COF of Cu/h-BN composites compacted at 700 MPa and sintered at 950 °C for 2 h at sliding speed of 0.2 m s^{-1} and 30 N load; (**f**) Wear rate of Cu/h-BN composites compacted under 700 MPa and sintered at 950 °C for 2 h at sliding speed 0.2 m s^{-1} (Reprinted with permission from Elsevier, Copyrights 2015) [155].

Tribological behavior of BN nano-platelet (BNNP) reinforced Ni_3Al intermetallic matrix composite has also been researched [159]. The result of a ball-on-disk wear testing revealed a good wear resistance of Ni_3Al/h-BN with a COF of 0.22–0.26 while pure Ni_3Al showed the range of 0.29–0.33. The ultimate anti-friction and high wear resistivity of the composites was shown to be high, attributing to the higher density of dislocation, mainly Orowan's mechanism [160] in which BNNPs are pulled out and bridged [12] (Figure 19e). As a result, lower shear stress associated with the addition of BNNPs and their self-lubrication characteristic enhanced the weight loss resistance. Figure 19f illustrates the

worn surface of neat Ni_3Al containing large debris, while the finer particles in debris on the worn surface of the composite can be seen, causing a lower wear rate [159]. In another research, the high temperature tribological properties of Ni-based self-lubricating coatings deposited by atmospheric plasma sprayed coating were studied [161]. The outcomes displayed that the COF and wear rate of the samples containing 5 wt.% and 10 wt.% of h-BN decrease when the temperatures is elevating up to 800 °C (Figure 19h). They reported that a smooth tribo-layer of lubricious phases is formed as a result of synergetic action of h-BN in the coating, and consequently, there will be no direct contact between the wear surface and the sliding ball [162]. As result of this tribo-layer, the minimum friction coefficient of 0.23 achieved where 10 wt.% of h-BN could reduce this parameter to 0.27 compared to the amount of 0.32 for the composite without h-BN [161].

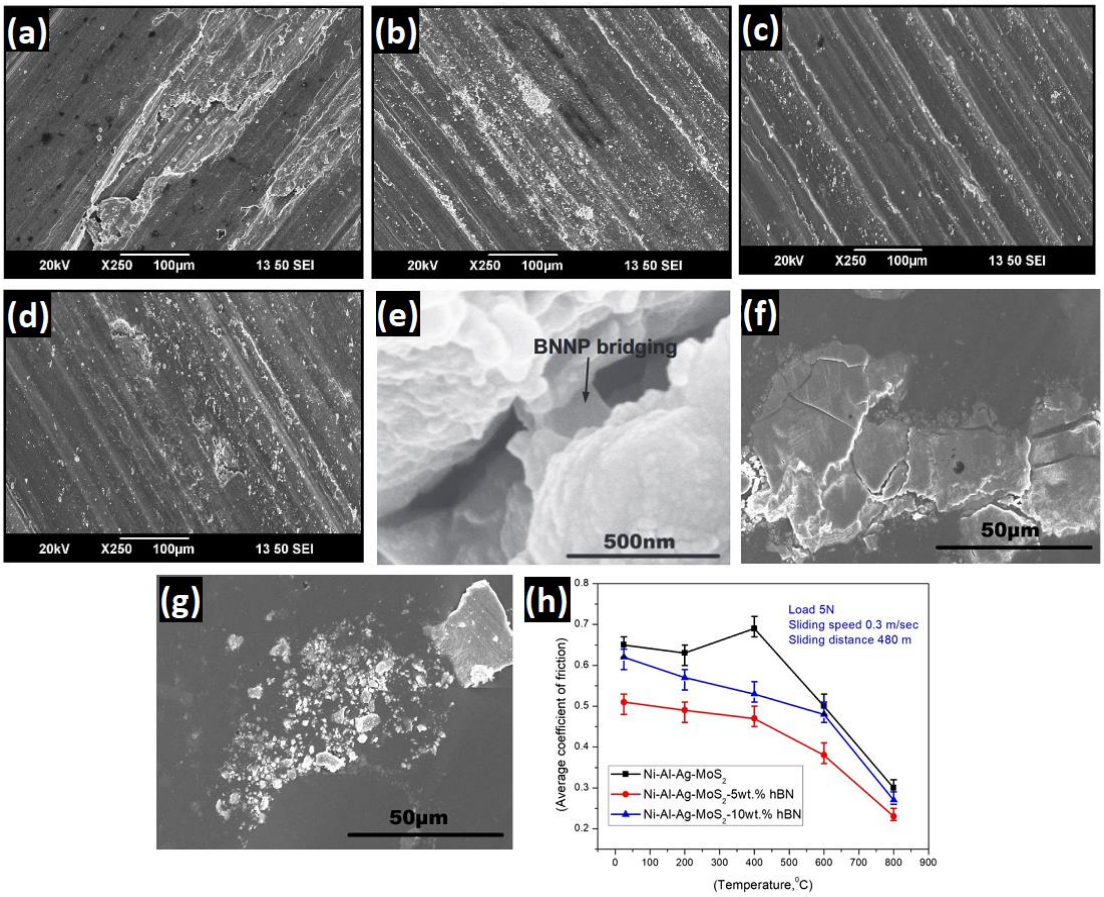

Figure 19. SEM micrograph of worn surface of; pure AA6082 (**a**) and AA6082 composite containing; TiB_2 (**b**), TiB_2 + h-BN (**c**), h-BN particles (**d**) (Reprinted with permission from Elsevier, Copyrights 2016) [156]. SEM images of BNNP bridging on the worn surface (**e**), wear debris of the Ni_3Al sample (**f**) and the BNNP/Ni_3Al composite at 9 N (**g**) (Reprinted with permission from Elsevier, Copyrights 2019) [159]. (**h**) Variation of average coefficient of friction with temperature for composite coatings (Reprinted with permission from Elsevier, Copyrights 2019) [161].

Hammes et al. has investigated the impact of h-BN and graphite on the mechanical scuffing resistance of self-lubricating iron-based composite [163]. They revealed that formation of a tribo-layer on the worn surface containing both graphite and h-BN can upgrade the composite wear resistance. Figure 20a shows the role of total lubricant amount on COF. As is shown, where the COF with total 5% of lubricant is around 0.3; having total 7.5% and 10% of lubricant can reduce the COF to 0.09 and 0.75 respectively. In all these samples, 1% of total amount of lubricant was h-BN. At the same point, 2.5% of h-BN in total 10% of lubricant leads to a COF of about 0.88. This reduction in COF can be attributed to the probability of formation of an oxide layer due to tribo-chemical reaction. The presence of both

h-BN and graphite provides a good source of solid lubricant and higher volume of this source supports the formation of the layer [164]. Further increase in h-BN content of lubricant leads to a higher COF, because of remains following the removal of materials on the wear surface. However, lower proportions of h-BN in the mixtures enhanced mechanical properties. Figure 20b exhibits mechanical strengths for the composite with different wt.% of lubricant as well as different vol.% of h-BN and graphite. In each group reduction in tensile strength with higher volume of h-BN is clearly shown. For instance, in total amount of 10% lubricant, with 1% h-BN the tensile strength is 225 MPa while 1.75% and 2.5% of h-BN in lubricant drop it to 170 and 155 MPa, respectively. Considering 1% h-BN in lubricant, for 5% of total lubricant, tensile strength is 285 MPa. While this amount is 250 MPa for 7.5% of lubricant and 225 MPa for 10% of it. This may be due to the discontinuity which occurs in matrix as a result of having solid lubricants [165]. Consequently, the best mechanical and simultaneously tribological improvement can be achieved in 1 vol.% of h-BN and 9 vol.% of graphite [163]. The recent developments in h-BN reinforced composites for tribological applications is summarized in Table 2.

3.2. Lubrication Additive

Except enhancing the tribological properties of metal, ceramic, and polymer matrices, h-BN can be used as lubrication additive in water or oil [131,166–168]. In one investigation, benefiting from different synthesis routs and treatments, BNNSs with different microstructure and sizes were obtained [169]. The samples obtained from route 2 (Equation (10)) were characterized by thin and small surface area, in contrast, the BNNSs of route 1 (Equation (9)) were relatively thicker and larger. Utilizing them as the lubrication additive in water revealed that the COF of bulk h-BN is near to pure water within the sliding test. In the case of BNNSs, the results become different; the behavior of all the samples became approximately the same till 500 s. Afterwards, up to 1800 s, the COF of BNNSs-2 and BNNSs-A gradually increased, whereas BNNSs-1 kept its COF low (Figure 20c). The possible reason is declared as poor mechanical strength of BNNSs-2 and BNNSs-A, which easily could be broken under applying high loads. However, thick and large BNNSs-1 can tolerate higher loads. The reason behind not appropriate performance of bulk h-BN can be the poor dispersion in water. The wear rate variation of the samples was seen similar to the COF behaviors. It can be concluded that the size of nanoparticles strongly affects the tribological properties of materials. Typically, size reduction should result in lowering wear resistance since a high density of defects is introduced to the structure and degrades the mechanical properties.

$$\text{Route 1 } (R_1): \; H_3BO_3 + Zn(CH_3COO)_2 \xrightarrow{\text{air, 900 °C, 3h}} Zn_3(BO_3)_2 + ZnO \xrightarrow{NH_3,\ 1200\ °C,\ 3h} BNNSs - 1 \tag{9}$$

$$\text{Route 2 } (R_2): \; H_3BO_3 + Zn(CH_3COO)_2 \xrightarrow{NH_3,\ 1200\ °C,\ 3h} BNNSs - 2 \xrightarrow{\text{air, 800 °C, 1h}} BNNSs - A \tag{10}$$

In an investigation, composite nanostructure of graphene and BNNSs was utilized to enhance the friction-reducing and anti-wear lubrication performance of oil [170]. This nanoparticles with diameter of larger than 200 nm and thickness of 10 nm were synthesized via high-energy ball milling for 20 h. The result of this harsh process was a flexible layered structure which can decrease the COF significantly and the wear scar diameters through providing mending and polishing effect (Figure 20d,e). It is worthy to note that the higher duration of ball milling caused reduction in the size of nanosheets, promoting forming an inflexible and agglomerated nanosheets. Surprisingly, benefiting computational calculations it was predicted that a large enough heterostructure of graphene/h-BN can lead to a low COF [31].

To show the excellent tribological properties of h-BN due to the interlayer slip, Xiaojing et al. used it as lubricant additive to Gas to Liquid-8 (GTL-8) as base oil [171]. Boron Nitride nanosheets were synthetized by molten alkali-assisted exfoliation and the mixture (2.84 g NaOH, 2.16 g KOH and 1 gr h-BN) was maintained in reactor for 2 and 6 h in 180 °C, and samples were respectively named BNNS-1

and BNNS-2. This increasing of exfoliation time led to declining the thickness from about 150 nm for raw h-BN to 45 and 3 nm for BNNS-1 and BNNS-2, respectively. The tribological assessments revealed that utilizing 0.3 mg mL^{-1} BNNS-1 in GTL-8 has represented the best performance by roughly 35% and 95% reduction in COF and wear volume, respectively. Figure 20f–h exhibits the wear surface taken by TEM. In the case of BNNS-1, a tribo-film can be observed with a thickness of 150 nm, as it is marked in Figure 20f. The same way in Figure 20g,h formed tribo-film with the thickness of 50 nm and 40 nm are shown in wear surface of h-BN and BNNS-2, respectively. The thick tribo-film of 150 nm corresponds to superior performance of BNNS-1. Also, having some wear debris on the worn surface as black pits can prove that the wear mechanism was abrasive [172]. For better understanding the role of BNNS, as shown in Figure 20i, we can consider them as a high-velocity rail which provides BNNS-1, simultaneously the oil molecules bring BNNS-1 and introduce them to the rubbing interface, leading to formation of a thick tribo-film. The problem with raw h-BN is its high thickness which cause cannot enter to the contact surface easily. So, the thickness of BNNS as a lubricant additive plays a crucial role in tribological behavior of oil-based lubricants.

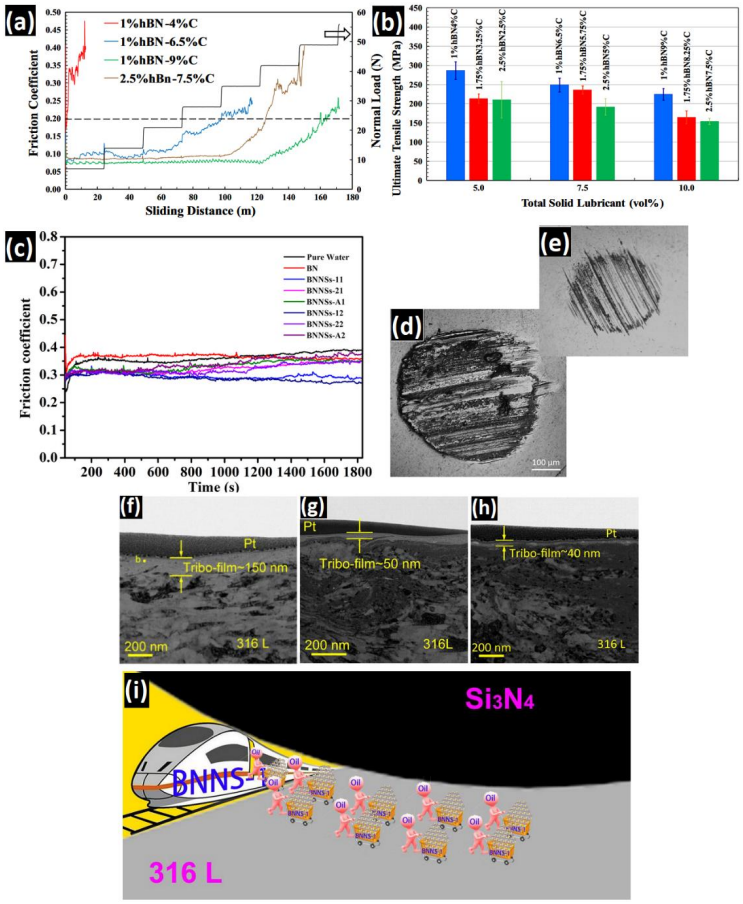

Figure 20. (**a**) Typical evolution of the COF with sliding distance, comparing the effect of total solid lubricant amount (5, 7.5, and 10 vol.%) and effect of h-BN content (1 and 2.5 vol.%), and (**b**) ultimate tensile strength of the sintered composites as function of the solid lubricant content (Reprinted with permission from Elsevier, Copyrights 2017) [163]. (**c**) COF curves of pure water, 0.5 mg mL^{-1} h-BN/water and BNNSs/water dispersions. The tribological tests were carried out at 100 N and 25 Hz, with an amplitude of 1 mm (Reprinted with permission from Elsevier, Copyrights 2019) [169]. Optical microscopy images of wear scars of the steel balls tested in (**d**) neat base oil and (**e**) base oil with graphene/h-BN composite nanosheets (four-ball method, 1770 rpm, 392 N, 10 s) (Reprinted with permission from WILEY-VCH, Copyrights 2018) [170]. Wear surface of (**f**) BNNS-1, (**g**) h-BN, and (**h**) BNNS-2; (**i**) illustration of friction mechanism (Reprinted with permission from Elsevier, Copyrights 2020) [171].

In another study, in order to compensate the poor dispersibility of h-BN in oil-based lubricant, firstly, h-BN was exfoliated and then fully oxidized to form hydroxyl functional groups [173]. Then, through the hydroxyl groups long alkyl chain carrying octadecyltriethoxysilane (ODTES) were chemically attached to BNNSs (Figure 21a). BNNS-ODTES was completely stable in synthetic polyol ester lube base oil owing to van der Waals interaction between the alkyl groups of polyol ester and octadecyl chains of BNNS-ODTES. Tribological evaluations indicated positive effect of BNNS-ODTES as an additive on wear behavior of synthetic polyol ester lubricant. For instance, studying wear track profile of steel disc which was lubricated with polyol ester without and with 0.04 mg mL^{-1} BNNS-ODTES depicted that BNNS-ODTES significantly reduced the wear width (from 570 to 345 µm) and depth (from 12.9 to 5.2 µm) (Figure 21b–d). The shear-induced delamination of the BNNS-ODTES and subsequent formation of a transfer film on the rubbing surface can be responsible for reducing wear [173]. Thus h-BN related materials can efficiently improve tribological behavior of components and enhance their performance.

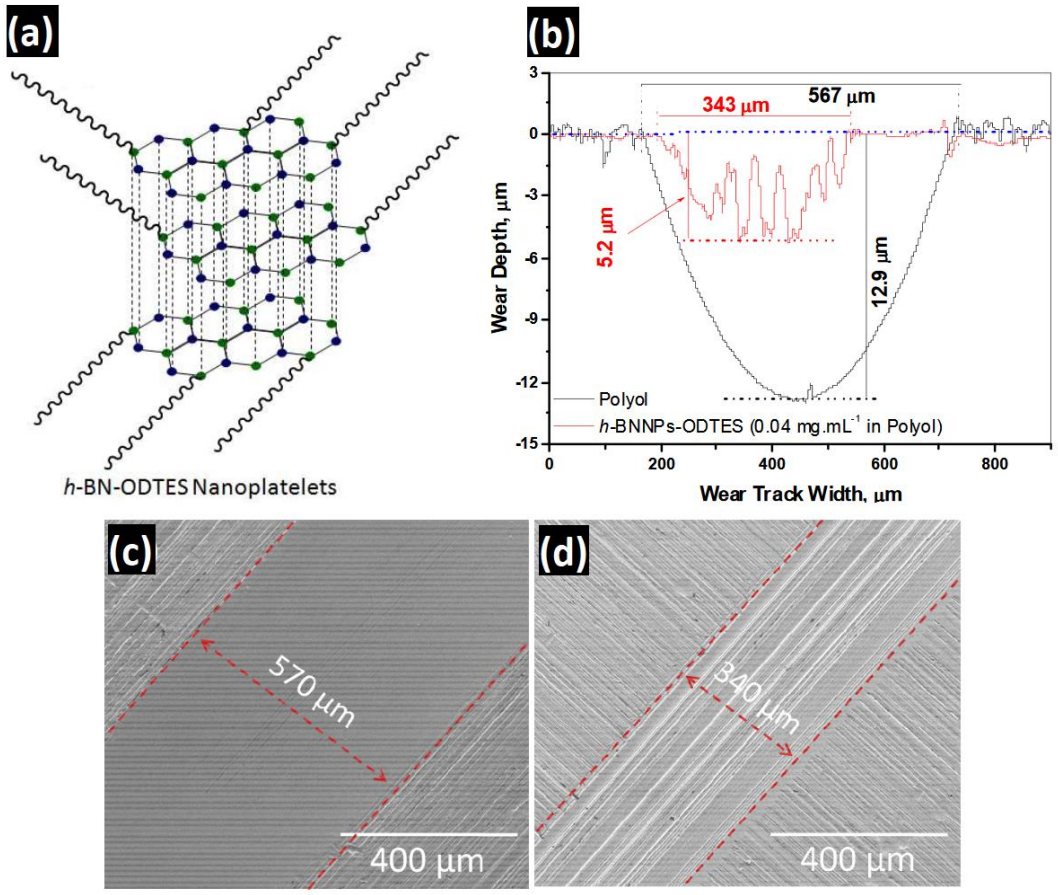

Figure 21. (**a**) Schematic of BNNS-ODTES structure. (**b**) Wear parameters of polyol ester lube oil with and without h-BNNPs-ODTES (concentration: 0.04 mg mL^{-1}) under bi-directional sliding contact. Load: 2 N; speed: 3 $cm{\cdot}sec^{-1}$, sliding distance: 100 m. Microscopic images of worn track on the steel disc after the lubrication tests under the 2N load. Prior to microscopic analyses, steel discs were thoroughly washed to remove the physisorbed content on the materials. (**c**) Lubricated with polyol ester and (**d**) lubricated with of h-BNNPs-ODTES blended polyol ester (dose: 0.04 mg mL^{-1}) (Reprinted with permission from American Chemical Society, Copyrights 2015) [173].

Table 2. Summary of recent developments in composites reinforced with h-BN for enhancing tribological properties.

Matrix	Filler & Content	Procedure	COF	Wear Rate	Other Features	Ref.
Poly aryl ether ketone (PAEK)	h-BN (10 wt.%)	Hot air circling and injection molding	Minimum COF was shown in composite with 10 wt.% of h-BN	Minimum wear rate was shown in composite with 10 wt.% of h-BN	Self-lubrication nature of BN	[174]
PAEK	h-BN in a combination of micro 7% and nano 3%	Magnetic stirring and injection molding	With micro h-BN = 0.055 With micro and nano h-BN = 0.046	-	Fiber damage in micron size. Flat surface of fiber and no de-bonding of fibers in nano size	[143]
Epoxy	Nano h-BN (1 wt.%)	Liquid casting method	Lowest COF at 1 wt.% h-BN which was 0.48	Lowest wear rate at 1 wt.% h-BN which was 3×10^{-5} $mm^3 \cdot N^{-1} \cdot m^{-1}$	Restricting crack development by BN and higher lubricity	[175]
Epoxy	0.5 wt.% of c-BN and h-BN	Exfoliation and ultrasonic treatment	COF with 0.5 wt.% c-BN/Epoxy: 9.74% lower than epoxy COF with 0.5 wt.% h-BN/Epoxy: 12.4% lower than epoxy	Wear rate of 0.5 wt.% c-BN/epoxy: 5.6×10^{-4} $mm^3 \cdot N^{-1} \cdot m^{-1}$ Wear rate of 0.5 wt.% h-BN/epoxy: 5.88×10^{-4} $mm^3 \cdot N^{-1} \cdot m^{-1}$ Wear rate of epoxy: 22.28×10^{-4} $mm^3 \cdot N^{-1} \cdot m^{-1}$	Removing direct contact between sliding surfaces and less adhesive wear	[140]
Epoxy	h-BN and c-BN	Heat treated, centrifuged, and dried in furnace	In dry sliding with h-BN = 0.62 In dry sliding with c-BN = 0.73	Wear rate in dry sliding with h-BN was higher than c-BN	Lower wear rate with c-BN is due to its hardness and hard particles of it in sliding interface increases the COF	[141]
Polyoxymethylene (POM)	3% h-BN (POM/10CF-3h-BN)	Hot press and heating at 190 °C	With 3% h-BN was between 0.13 to 0.14 in different loadings	Wear rate with 3% h-BN = 6.3×10^{-7} $mm^3 \cdot N^{-1} \cdot m^{-1}$	Synergetic role of h-BN and carbon fiber	[137]
B_4C	h-BN (20 wt.%)	Hot press sintering under 350 MPa at 1800 °C for 60 min	Without h-BN = 0.38 With 20 wt.% h-BN = 0.005	Lowest wear rate was shown in 20 wt.% of h-BN	Formation of a tribo-film on the wearing surface	[29]
B_4C	h-BN (30 wt.%)	Hot press sintering under 350 MPa at 1800 °C, for 60 min	Without h-BN = 0.58 With 30 wt.% h-BN = 0.38	Lower wear coefficient with increasing h-BN content; Lowest wear coefficient in 30 wt.% of h-BN	Formation of a transfer film on the wearing surface, the reduction of the percentage of hard particles	[176]
Si_3N_4	h-BN (20 wt.%)	Hot press sintering under 30 MPa at 1800 °C for dwell time of 30 min	Without h-BN = 0.58 With 20 wt.% h-BN = 0.302	Minimum wear rate was 2.93×10^{-6} $mm^3 \cdot N^{-1} \cdot m^{-1}$ in 20 wt.% of h-BN	Forming a tribo-chemical film in contact surface of sliding pair	[150]
Si_3N_4	h-BN (20 wt.%)	Hot pressing	Without h-BN = 0.58 With 20 wt.% h-BN = 0.31	Lowest wear rate at 20 wt.% h-BN	Forming a tribo-film of metal oxide	[177]
c-BN	h-BN (5 to 15 wt.%)	Ball mixing for 30 min and sintering at 880 °C for 30 min	With 5 wt.% h-BN = 0.7 With 15 wt.% h-BN = 0.3	Wear volume in 5 wt.% h-BN = 0.126 $mm^3 \cdot N^{-1} \cdot m^{-1}$ wear volume in 15 wt.% h-BN = 0.135 $mm^3 \cdot N^{-1} \cdot m^{-1}$	Forming a tribo-layer in friction interface	[148]

Table 2. *Cont.*

Matrix	Filler & Content	Procedure	COF	Wear Rate	Other Features	Ref.
CNT	$h\text{-}BN_{0.75}C_{0.25}$, $h\text{-}BN_{0.5}C_{0.5}$, $h\text{-}_{.25}C_{0.75}$	Covalent crosslinking	Lowest COF was shown in $BN_{0.5}C_{0.5}$	Lowest wear rate achieved for $BN_{0.5}C_{0.5}$	Smooth worn surface due to a tribo-film	[151]
AA6082	TiB_2 and h-BN (50% TiB_2 + 50% h-BN)	Friction stir processing	Lower COF with increasing h-BN	Wear rate of AA6082 = 23.75×10^{-5} $mm^3 \cdot N^{-1} \cdot m^{-1}$ wear rate of AA6082/50% TiB_2 + 50% h-BN = 13×10^{-5} $mm^3 \cdot N^{-1} \cdot m^{-1}$	Change of wear mechanism from adhesive to abrasive due to TiB2 and BN in the wear interface	[156]
Fe–Si–C	h-BN and graphite (10% of lubricant containing h-BN: 1 vol.% and graphite: 9 vol.%)	Isothermal sintering at 500 °C for 30 min	Lowest COF in the composite with 1 vol.% of h-BN and 9 vol.% of graphite	An improvement in wear resistance in the composite with 1 vol.% of h-BN and 9 vol.% of graphite	Formation of a oxide layer due to tribo-chemical reaction	[163]
Ni–Ag–Al–MoS_2	h-BN (5 wt.%)	Ball milling for 8 h at 200 rpm	Without = 0.32 With 5 wt.% h-BN = 0.23	Lowest wear rate was found in 5 wt.% h-BN	No direct contact between sliding pair due to a tribo-layer formation	[161]
Ni60	Nano-Cu and h-BN (from room temperature to 600 °C)	Ball milling for 3 h at 300 rpm, Laser cladding at 3 kW and scanning speed of 2 mm s^{-1}	At all temperatures: minimum COF was found with nano-Cu and h-BN lubricant and it was 0.323 at 600 °C	At all temperatures Ni60 with nano-Cu and h-BN lubricant showed the minimum wear rate	Change of wear mechanism from abrasive to adhesive above 400 °C	[178]
Ni_3Al	h-BN nano plate (BNNP)	Electrostatic absorption dispersion method	Without BNNP = 0.30 With BNNP = 0.22	Depth of wear track for Ni_3Al = 0.35 µm, depth of wear track for Ni_3Al/BNNP = 0.28 µm	Weight loss resistance due to self-lubrication characteristic	[159]
Al6061	h-BN and Al_2O_3 (30 h-BN-10 Al_2O_3-5 C)	Stir casting	-	Lowest wear rate for 30 h-BN-10 Al_2O_3-5 C due to hard h-BN and Al_2O_3 particles reinforcement	Self-lubrication nature of BN and C. Wear mechanism was adhesive.	[179]
Co	10 wt.% h-BN	Ball milling and cladding on a die steel sheet	Without h-BN = 0.52 With 10 wt.% h-BN = 0.422	Wear rate with 10 wt.% h-BN = 7.5×10^{-5} $mm^3 \cdot N^{-1} \cdot m^{-1}$ Wear rate with 10 wt.% h-BN = 24.9×10^{-5} $mm^3 \cdot N^{-1} \cdot m^{-1}$	Improvement in lubricity and changing the wear mechanism due to lubricating characteristic of h-BN	[180]
Cu	2.5 wt.% h-BN	Electroless deposition	Without h-BN = 0.37 with 2.5 wt.% h-BN = 0.008	Wear rate increases with higher amount of h-BN	Higher wear rate with addition of h-BN is due to the low shear strength. Reduction in COF attributes to lubricity of h-BN	[155]

4. Conclusions and Future Perspectives

To recapitulate, 2D h-BN nowadays encompasses almost all geographic borders of scientific realms with its outstanding properties including high TC, electrical insulation character with its tunable 5.9 eV band gap, excellent chemical/thermal stability, superior resistivity against corrosion/oxidation and being and intrinsically lubricant material as a result of its layered structure. To be more specific, having high TC and dielectric characteristics at the same time, arises numerous research interests in this material to be utilized as a reinforcement agent towards enhancing heat transfer quality of PMCs in the electronic packaging industry. Since h-BN is regarded as an anisotropic filler with a distinctive difference in its in-plane and out-plane TCs, the overall TC of the h-BN-reinforced polymer composite is correlated to filler's alignment in the polymer matrix, filler's functional groups, the quality of fillers dispersion and the effort in producing a continuous heat conduction path, filler-filler and filler-polymer interfacial properties. In addition, possessing atomic flatness, high aspect ratio, and crystallinity of h-BN favors efficient heat dissipation without the formation of localized hot spots. According to theoretical points of view, BNNSs takes precedence from bulk h-BN due to the suppressed phonon scattering in the few-layered materials. Thereby, many efforts have been devoted to controlling the orientation of h-BN platelets through synthesis techniques to exploit the ultimate potential of its high TC in polymer composites. Herein, we discussed comprehensively the most common techniques focused on orientation manipulating and incorporation of h-BN fillers which are freeze-drying, magnetic field/template-assisted, CVD, mechanical milling, and electrospinning. Apart from that, easy sliding layers, low friction coefficient as a result of low shear strength and ability to function in a wide range of environments such as wet/dry/oxidative/high temperatures have been favored in producing highly durable composites with increased wear resistance.

Despites of virtues and merits of h-BN in improving thermal properties and tribological behaviors of polymer/metal/CMCs, this research topic is still faced with some challenges that affects the overall performance of the final composite in their relevant applications and hinders h-BNs utilization in those fields. The first challenge is developing fully controlled BNNSs in terms of crystallinity, morphology, number of layers, functionalization and surface chemistry. The next one aims at the compatibility of the BNNSs-matrix interface that plays a crucial role in their correspondence application. Meticulous evaluation of these problems undoubtedly paves a new path for the utilization of h-BN in novel thermal and tribological applications where other materials could not enter and endure.

Author Contributions: Conceptualization, S.A.A.A. and S.A.; resources, S.A.A.A.; writing—original draft preparation, M.K., S.Z.G., S.A.A.A., K.B., and M.H.A.; writing—review and editing, S.A., M.K., S.A.A.A., and S.Z.G.; supervision, S.A. and M.K. All authors have read and agreed to the published version of the manuscript.

Funding: This research received no external funding.

Conflicts of Interest: The authors declare no conflict of interest.

References

1. Novoselov, K.S.; Geim, A.K.; Morozov, S.V.; Jiang, D.; Zhang, Y.; Dubonos, S.V.; Grigorieva, I.V.; Firsov, A.A. Electric Field Effect in Atomically Thin Carbon Films. *Science* **2004**, *306*, 666–669. [CrossRef] [PubMed]
2. Liu, X.; Ma, T.; Pinna, N.; Zhang, J. Two-Dimensional Nanostructured Materials for Gas Sensing. *Adv. Funct. Mater.* **2017**, *27*, 1702168. [CrossRef]
3. Zhang, X.; Lai, Z.; Tan, C.; Zhang, H. Solution-Processed Two-Dimensional MoS2Nanosheets: Preparation, Hybridization, and Applications. *Angew. Chemie Int. Ed. Engl.* **2016**, *55*, 8816–8838. [CrossRef] [PubMed]
4. Khalaj, M.; Sedghi, A.; Miankushki, H.N.; Golkhatmi, S.Z. Synthesis of novel graphene/Co3O4/polypyrrole ternary nanocomposites as electrochemically enhanced supercapacitor electrodes. *Energy* **2019**, *188*, 116088. [CrossRef]
5. Golkhatmi, S.Z.; Khalaj, M.; Izadpanahi, A.; Sedghi, A. One-step electrodeposition synthesis of high performance Graphene/Cu_2O nanocomposite films on copper foils as binder-free supercapacitor electrodes. *Solid State Sci.* **2020**, *106*, 106336. [CrossRef]

6. Gogotsi, Y.; Anasori, B. The Rise of MXenes. *ACS Nano* **2019**, *13*, 8491–8494. [CrossRef]
7. Anasori, B.; Lukatskaya, M.R.; Gogotsi, Y. 2D metal carbides and nitrides (MXenes) for energy storage. *Nat. Rev. Mater.* **2017**, *2*. [CrossRef]
8. Li, X.; Shan, J.; Zhang, W.; Su, S.; Yuwen, L.; Wang, L. Recent Advances in Synthesis and Biomedical Applications of Two-Dimensional Transition Metal Dichalcogenide Nanosheets. *Small* **2017**, *13*, 1602660. [CrossRef]
9. Bollella, P.; Fusco, G.; Tortolini, C.; Sanzò, G.; Favero, G.; Gorton, L.; Antiochia, R. Beyond graphene: Electrochemical sensors and biosensors for biomarkers detection. *Biosens. Bioelectron.* **2017**, *89*, 152–166. [CrossRef]
10. Zhang, K.; Feng, Y.; Wang, F.; Yang, Z.; Wang, J. Two dimensional hexagonal boron nitride (2D-hBN): Synthesis, properties and applications. *J. Mater. Chem. C.* **2017**, *5*, 11992–12022. [CrossRef]
11. Lin, Y.; Connell, J.W. Advances in 2D boron nitride nanostructures: Nanosheets, nanoribbons, nanomeshes, and hybrids with graphene. *Nanoscale* **2012**, *4*, 6908–6939. [CrossRef] [PubMed]
12. Guerra, V.; Wan, C.; McNally, T. Thermal conductivity of 2D nano-structured boron nitride (BN) and its composites with polymers. *Prog. Mater. Sci.* **2019**, *100*, 170–186. [CrossRef]
13. Yin, J.; Li, J.; Hang, Y.; Yu, J.; Tai, G.; Li, X.; Zhang, Z.; Guo, W. Boron Nitride Nanostructures: Fabrication, Functionalization and Applications. *Small* **2016**, *12*, 2942–2968. [CrossRef]
14. Giovannetti, G.; Khomyakov, P.A.; Brocks, G.; Kelly, P.J.; van den Brink, J. Substrate-induced band gap in graphene on hexagonal boron nitride: Ab initio density functional calculations. *Phys. Rev. B.* **2007**, *76*, 73103. [CrossRef]
15. Glavin, N.R.; Jespersen, M.L.; Check, M.H.; Hu, J.; Hilton, A.M.; Fisher, T.S.; Voevodin, A.A. Synthesis of few-layer, large area hexagonal-boron nitride by pulsed laser deposition. *Thin Solid Film* **2014**, *572*, 245–250. [CrossRef]
16. Meric, I.; Dean, C.R.; Petrone, N.; Wang, L.; Hone, J.; Kim, P.; Shepard, K.L. Graphene Field-Effect Transistors Based on Boron–Nitride Dielectrics. *Proc. IEEE* **2013**, *101*, 1609–1619. [CrossRef]
17. Fu, L.; Lai, G.; Chen, G.; Lin, C.-T.; Yu, A. Microwave Irradiation-Assisted Exfoliation of Boron Nitride Nanosheets: A Platform for Loading High Density of Nanoparticles. *Chem. Sel.* **2016**, *1*, 1799–1803. [CrossRef]
18. Li, L.H.; Chen, Y. Atomically Thin Boron Nitride: Unique Properties and Applications. *Adv. Funct. Mater.* **2016**, *26*, 2594–2608. [CrossRef]
19. Byun, S.; Kim, J.H.; Song, S.H.; Lee, M.; Park, J.J.; Lee, G.; Hong, S.H.; Lee, D. Ordered, Scalable Heterostructure Comprising Boron Nitride and Graphene for High-Performance Flexible Supercapacitors. *Chem. Mater.* **2016**, *28*, 7750–7756. [CrossRef]
20. Gao, T.; Gong, L.; Wang, Z.; Yang, Z.; Pan, W.; He, L.; Zhang, J.; Ou, E.; Xiong, Y.; Xu, W. Boron nitride/reduced graphene oxide nanocomposites as supercapacitors electrodes. *Mater. Lett.* **2015**, *159*, 54–57. [CrossRef]
21. Khan, A.F.; Down, M.P.; Smith, G.C.; Foster, C.W.; Banks, C.E. Surfactant-exfoliated 2D hexagonal boron nitride (2D-hBN): Role of surfactant upon the electrochemical reduction of oxygen and capacitance applications. *J. Mater. Chem. A* **2017**, *5*, 4103–4113. [CrossRef]
22. Angizi, S.; Hatamie, A.; Ghanbari, H.; Simchi, A. Mechanochemical Green Synthesis of Exfoliated Edge-Functionalized Boron Nitride Quantum Dots: Application to Vitamin C Sensing through Hybridization with Gold Electrodes. *ACS Appl. Mater. Interfaces* **2018**, *10*, 28819–28827. [CrossRef] [PubMed]
23. Ivanova, M.N.; Grayfer, E.D.; Plotnikova, E.E.; Kibis, L.S.; Darabdhara, G.; Boruah, P.K.; Das, M.R.; Fedorov, V.E. Pt-Decorated Boron Nitride Nanosheets as Artificial Nanozyme for Detection of Dopamine. *ACS Appl. Mater. Interfaces* **2019**, *11*, 22102–22112. [CrossRef] [PubMed]
24. Angizi, S.; Shayeganfar, F.; Azar, M.H.; Simchi, A. Surface/edge functionalized boron nitride quantum dots: Spectroscopic fingerprint of bandgap modification by chemical functionalization. *Ceram. Int.* **2020**, *46*, 978–985. [CrossRef]
25. Hatamie, A.; Rahmati, R.; Rezvani, E.; Angizi, S.; Simchi, A. Yttrium hexacyanoferrate microflowers on freestanding three-dimensional graphene substrates for ascorbic acid detection. *ACS Appl. Nano Mater.* **2019**, *2*, 2212–2221. [CrossRef]
26. Guo, Y.; Lyu, Z.; Yang, X.; Lu, Y.; Ruan, K.; Wu, Y.; Kong, J.; Gu, J. Enhanced thermal conductivities and decreased thermal resistances of functionalized boron nitride/polyimide composites. *Compos. Part B Eng.* **2019**, *164*, 732–739. [CrossRef]

27. Isarn, I.; Bonnaud, L.; Massagués, L.; Serra, À.; Ferrando, F. Enhancement of thermal conductivity in epoxy coatings through the combined addition of expanded graphite and boron nitride fillers. *Prog. Org. Coat.* **2019**, *133*, 299–308. [CrossRef]
28. Zhu, S.; Cheng, J.; Qiao, Z.; Yang, J. High temperature solid-lubricating materials: A review. *Tribol. Int.* **2019**, *133*, 206–223. [CrossRef]
29. Li, X.; Gao, Y.; Yang, Q.; Pan, W.; Li, Y.; Zhong, Z.; Song, L. Evaluation of tribological behavior of B4C—hBN ceramic composites under water-lubricated condition. *Ceram. Int.* **2015**, *41*, 7387–7393. [CrossRef]
30. Burger, N.; Laachachi, A.; Ferriol, M.; Lutz, M.; Toniazzo, V.; Ruch, D. Review of thermal conductivity in composites: Mechanisms, parameters and theory. *Prog. Polym. Sci.* **2016**, *61*, 1–28. [CrossRef]
31. Leven, I.; Krepel, D.; Shemesh, O.; Hod, O. Robust Superlubricity in Graphene/h-BN Heterojunctions. *J. Phys. Chem. Lett.* **2013**, *4*, 115–120. [CrossRef] [PubMed]
32. Yuan, C.; Li, J.; Lindsay, L.; Cherns, D.; Pomeroy, J.W.; Liu, S.; Edgar, J.H.; Kuball, M. Modulating the thermal conductivity in hexagonal boron nitride via controlled boron isotope concentration. *Commun. Phys.* **2019**, *2*, 1–8. [CrossRef]
33. Zhang, Y.F.; Chen, L.; Ge, Y.Y.; Wang, Q.Y.; Bai, S.L. Graphite tube woven fabric/boron nitride/polymer composite with enhanced thermal conductivity and electric isolation. *Polym. Compos.* **2019**, *40*, E1808–E1817. [CrossRef]
34. Pakdel, A.; Bando, Y.; Golberg, D. Nano boron nitride flatland. *Chem. Soc. Rev.* **2014**, *43*, 934–959. [CrossRef]
35. Park, O.K.; Owuor, P.S.; Jaques, Y.M.; Galvao, D.S.; Kim, N.H.; Lee, J.H.; Tiwary, C.S.; Ajayan, P.M. Hexagonal boron nitride-carbon nanotube hybrid network structure for enhanced thermal, mechanical and electrical properties of polyimide nanocomposites. *Compos. Sci. Technol.* **2020**, *188*, 107977. [CrossRef]
36. Paszkiewicz, S.; Taraghi, I.; Szymczyk, A.; Huczko, A.; Kurcz, M.; Przybyszewski, B.; Stanik, R.; Linares, A.; Ezquerra, T.A.; Rosłaniec, Z. Electrically and thermally conductive thin elastic polymer foils containing SiC nanofibers. *Compos. Sci. Technol.* **2017**, *146*, 20–25. [CrossRef]
37. Shen, D.; Zhan, Z.; Liu, Z.; Cao, Y.; Zhou, L.; Liu, Y.; Dai, W.; Nishimura, K.; Li, C.; Lin, C.T.; et al. Enhanced thermal conductivity of epoxy composites filled with silicon carbide nanowires. *Sci. Rep.* **2017**, *7*, 1–11. [CrossRef]
38. Yin, L.; Zhou, X.; Yu, J.; Wang, H.; Ran, C. Fabrication of a polymer composite with high thermal conductivity based on sintered silicon nitride foam. *Compos. Part A Appl. Sci. Manuf.* **2016**, *90*, 626–632. [CrossRef]
39. Akhtar, M.W.; Lee, Y.S.; Yoo, D.J.; Kim, J.S. Alumina-graphene hybrid filled epoxy composite: Quantitative validation and enhanced thermal conductivity. *Compos. Part B Eng.* **2017**, *131*, 184–195. [CrossRef]
40. Li, S.; Feng, Y.; Li, Y.; Feng, W.; Yoshino, K. Transparent and flexible films of horizontally aligned carbon nanotube/polyimide composites with highly anisotropic mechanical, thermal, and electrical properties. *Carbon N. Y.* **2016**, *109*, 131–140. [CrossRef]
41. Xu, L.; Chen, G.; Wang, W.; Li, L.; Fang, X. A facile assembly of polyimide/graphene core-shell structured nanocomposites with both high electrical and thermal conductivities. *Compos. Part A Appl. Sci. Manuf.* **2016**, *84*, 472–481. [CrossRef]
42. Cho, H.B.; Konno, A.; Fujihara, T.; Suzuki, T.; Tanaka, S.; Jiang, W.; Suematsu, H.; Niihara, K.; Nakayama, T. Self-assemblies of linearly aligned diamond fillers in polysiloxane/diamond composite films with enhanced thermal conductivity. *Compos. Sci. Technol.* **2011**, *72*, 112–118. [CrossRef]
43. Ji, T.; Feng, Y.; Qin, M.; Li, S.; Zhang, F.; Lv, F.; Feng, W. Thermal conductive and flexible silastic composite based on a hierarchical framework of aligned carbon fibers-carbon nanotubes. *Carbon N. Y.* **2018**, *131*, 149–159. [CrossRef]
44. Li, J.; Qi, S.; Li, J.; Zhang, M.; Wang, Z. A highly thermostable and transparent lateral heat spreader based on silver nanowire/polyimide composite. *RSC Adv.* **2015**, *5*, 59398–59402. [CrossRef]
45. Yu, S.; Lee, J.W.; Han, T.H.; Park, C.; Kwon, Y.; Hong, S.M.; Koo, C.M. Copper shell networks in polymer composites for efficient thermal conduction. *ACS Appl. Mater. Interfaces.* **2013**, *5*, 11618–11622. [CrossRef] [PubMed]
46. Chung, S.; Im, Y.; Kim, H.; Park, S.; Jeong, H. Evaluation for micro scale structures fabricated using epoxy-aluminum particle composite and its application. *J. Mater. Process. Technol.* **2005**, *160*, 168–173. [CrossRef]

47. Duan, G.; Wang, Y.; Yu, J.; Zhu, J.; Hu, Z. Improved thermal conductivity and dielectric properties of flexible PMIA composites with modified micro- and nano-sized hexagonal boron nitride. *Front. Mater. Sci.* **2019**, *13*, 64–76. [CrossRef]
48. Yang, D.; Ni, Y.; Kong, X.; Gao, D.; Wang, Y.; Hu, T.; Zhang, L. Mussel-inspired modification of boron nitride for natural rubber composites with high thermal conductivity and low dielectric constant. *Compos. Sci. Technol.* **2019**, *177*, 18–25. [CrossRef]
49. Zhang, R.H.; Shi, X.T.; Tang, L.; Liu, Z.; Zhang, J.L.; Guo, Y.Q.; Gu, J.W. Thermally Conductive and Insulating Epoxy Composites by Synchronously Incorporating Si-sol Functionalized Glass Fibers and Boron Nitride Fillers. *Chin. J. Polym. Sci.* **2020**, *38*, 730–739. [CrossRef]
50. Lewis, J.S.; Barani, Z.; Magana, A.S.; Kargar, F.; Balandin, A.A. Thermal and electrical conductivity control in hybrid composites with graphene and boron nitride fillers. *Mater. Res. Express.* **2019**, *6*, 085325. [CrossRef]
51. Mai, V.D.; Lee, D.-I.; Park, J.H.; Lee, D.S. Rheological properties and thermal conductivity of epoxy resins filled with a mixture of alumina and boron nitride. *Polymers* **2019**, *11*, 597. [CrossRef] [PubMed]
52. Han, J.; Du, G.; Gao, W.; Bai, H. An Anisotropically High Thermal Conductive Boron Nitride/Epoxy Composite Based on Nacre-Mimetic 3D Network. *Adv. Funct. Mater.* **2019**, *29*, 1–9. [CrossRef]
53. Hou, X.; Chen, Y.; Lv, L.; Dai, W.; Zhao, S.; Wang, Z.; Fu, L.; Lin, C.T.; Jiang, N.; Yu, J. High-Thermal-Transport-Channel Construction within Flexible Composites via the Welding of Boron Nitride Nanosheets. *ACS Appl. Nano Mater.* **2019**, *2*, 360–368. [CrossRef]
54. Wang, J.; Liu, D.; Li, Q.; Chen, C.; Chen, Z.; Song, P.; Hao, J.; Li, Y.; Fakhrhoseini, S.; Naebe, M.; et al. Lightweight, Superelastic Yet Thermoconductive Boron Nitride Nanocomposite Aerogel for Thermal Energy Regulation. *ACS Nano* **2019**. [CrossRef] [PubMed]
55. Wang, X.; Wu, P. Preparation of Highly Thermally Conductive Polymer Composite at Low Filler Content via a Self-Assembly Process between Polystyrene Microspheres and Boron Nitride Nanosheets. *ACS Appl. Mater. Interfaces* **2017**, *9*, 19934–19944. [CrossRef] [PubMed]
56. Nagaoka, S.; Jodai, T.; Kameyama, Y.; Horikawa, M.; Shirosaki, T.; Ryu, N.; Takafuji, M.; Sakurai, H.; Ihara, H. Cellulose/boron nitride core–shell microbeads providing high thermal conductivity for thermally conductive composite sheets. *RSC Adv.* **2016**, *6*, 33036–33042. [CrossRef]
57. Sun, J.; Wang, D.; Yao, Y.; Zeng, X.; Pan, G.; Huang, Y.; Hu, J.; Sun, R.; Xu, J.; Wong, C. Boron nitride microsphere/epoxy composites with enhanced thermal conductivity. *High Volt.* **2017**, *2*, 147–153. [CrossRef]
58. Xiao, C.; Tang, Y.; Chen, L.; Zhang, X.; Zheng, K.; Tian, X. Preparation of highly thermally conductive epoxy resin composites via hollow boron nitride microbeads with segregated structure. *Compos. Part A Appl. Sci. Manuf.* **2019**, *121*, 330–340. [CrossRef]
59. Zhu, Z.; Li, C.; Songfeng, E.; Xie, L.; Geng, R.; Lin, C.T.; Li, L.; Yao, Y. Enhanced thermal conductivity of polyurethane composites via engineering small/large sizes interconnected boron nitride nanosheets. *Compos. Sci. Technol.* **2019**, *170*, 93–100. [CrossRef]
60. Wang, H.; Ding, D.; Liu, Q.; Chen, Y.; Zhang, Q. Highly anisotropic thermally conductive polyimide composites via the alignment of boron nitride platelets. *Compos. Part B Eng.* **2019**, *158*, 311–318. [CrossRef]
61. Tian, C.; Yuan, L.; Liang, G.; Gu, A. High thermal conductivity and flame-retardant phosphorus-free bismaleimide resin composites based on 3D porous boron nitride framework. *J. Mater. Sci.* **2019**, *54*, 7651–7664. [CrossRef]
62. Yuan, J.; Qian, X.; Meng, Z.; Yang, B.; Liu, Z.Q. Highly Thermally Conducting Polymer-Based Films with Magnetic Field-Assisted Vertically Aligned Hexagonal Boron Nitride for Flexible Electronic Encapsulation. *ACS Appl. Mater. Interfaces* **2019**, *11*, 17915–17924. [CrossRef] [PubMed]
63. Xue, Y.; Li, X.; Wang, H.; Zhao, F.; Zhang, D.; Chen, Y. Improvement in thermal conductivity of through-plane aligned boron nitride/silicone rubber composites. *Mater. Des.* **2019**, *165*, 107580. [CrossRef]
64. Liang, W.; Ge, X.; Ge, J.; Li, T.; Zhao, T.; Chen, X.; Zhang, M.; Ji, J.; Pang, X.; Liu, R. Three-dimensional heterostructured reduced graphene oxide-hexagonal boron nitride-stacking material for silicone thermal grease with enhanced thermally conductive properties. *Nanomaterials* **2019**, *9*, 938. [CrossRef] [PubMed]
65. Lin, Z.; Liu, Y.; Raghavan, S.; Moon, K.; Sitaraman, S.K.; Wong, C. Magnetic Alignment of Hexagonal Boron Nitride Platelets in Polymer Matrix: Toward High Performance Anisotropic Polymer Composites for Electronic Encapsulation. *ACS Appl. Mater. Interfaces* **2013**, *5*, 7633–7640. [CrossRef] [PubMed]

66. Yuan, C.; Duan, B.; Li, L.; Xie, B.; Huang, M.; Luo, X. Thermal Conductivity of Polymer-Based Composites with Magnetic Aligned Hexagonal Boron Nitride Platelets. *ACS Appl. Mater. Interfaces* **2015**, *7*, 13000–13006. [CrossRef] [PubMed]
67. Yuan, C.; Li, L.; Duan, B.; Xie, B.; Zhu, Y.; Luo, X. Locally reinforced polymer-based composites for efficient heat dissipation of local heat source. *Int. J. Therm. Sci.* **2016**, *102*, 202–209. [CrossRef]
68. Li, Y.; Tian, X.; Yang, W.; Li, Q.; Hou, L.; Zhu, Z.; Tang, Y.; Wang, M.; Zhang, B.; Pan, T.; et al. Dielectric composite reinforced by in-situ growth of carbon nanotubes on boron nitride nanosheets with high thermal conductivity and mechanical strength. *Chem. Eng. J.* **2019**, *358*, 718–724. [CrossRef]
69. Chen, J.; Huang, X.; Sun, B.; Wang, Y.; Zhu, Y.; Jiang, P. Vertically Aligned and Interconnected Boron Nitride Nanosheets for Advanced Flexible Nanocomposite Thermal Interface Materials. *ACS Appl. Mater. Interfaces* **2017**, *9*, 30909–30917. [CrossRef]
70. Agari, Y.; Ueda, A.; Nagai, S. Thermal conductivity of a polymer composite. *J. Appl. Polym. Sci.* **1993**, *49*, 1625–1634. [CrossRef]
71. Xiao, Y.; Wang, W.; Lin, T.; Chen, X.; Zhang, Y.; Yang, J.; Wang, Y.; Zhou, Z. Largely enhanced thermal conductivity and high dielectric constant of poly (vinylidene fluoride)/boron nitride composites achieved by adding a few carbon nanotubes. *J. Phys. Chem. C* **2016**, *120*, 6344–6355. [CrossRef]
72. Feng, Y.; Han, G.; Wang, B.; Zhou, X.; Ma, J.; Ye, Y.; Liu, C.; Xie, X. Multiple synergistic effects of graphene-based hybrid and hexagonal born nitride in enhancing thermal conductivity and flame retardancy of epoxy. *Chem. Eng. J.* **2020**, *379*, 122402. [CrossRef]
73. Mosanenzadeh, S.G.; Khalid, S.; Cui, Y.; Naguib, H.E. High thermally conductive PLA based composites with tailored hybrid network of hexagonal boron nitride and graphene nanoplatelets. *Polym. Compos.* **2016**, *37*, 2196–2205. [CrossRef]
74. Azar, M.H.; Sadri, B.; Nemati, A.; Angizi, S.; Shaeri, M.H.; Minárik, P.; Veselý, J.; Djavanroodi, F. Investigating the microstructure and mechanical properties of aluminum-matrix reinforced- graphene nanosheet composites fabricated by mechanical milling and equal-channel angular pressing. *Nanomaterials* **2019**, *9*, 1070. [CrossRef]
75. Fan, Y.; Cho, U.R. Effects of graphite and boron nitride based fillers on mechanical, thermal conductive, and thermo-physical properties in solution styrene–butadiene rubber. *Polym. Compos.* **2019**, *40*, E1426–E1433. [CrossRef]
76. Yuan, F.-Y.; Zhang, H.-B.; Li, X.; Li, X.-Z.; Yu, Z.-Z. Synergistic effect of boron nitride flakes and tetrapod-shaped ZnO whiskers on the thermal conductivity of electrically insulating phenol formaldehyde composites. *Compos. Part A Appl. Sci. Manuf.* **2013**, *53*, 137–144. [CrossRef]
77. Liu, M.; Chiang, S.-W.; Chu, X.; Li, J.; Gan, L.; He, Y.; Li, B.; Kang, F.; Du, H. Polymer composites with enhanced thermal conductivity via oriented boron nitride and alumina hybrid fillers assisted by 3-D printing. *Ceram. Int.* **2020**. [CrossRef]
78. Yang, Q.; Zhang, Z.; Gong, X.; Yao, E.; Liu, T.; Zhang, Y.; Zou, H. Thermal conductivity of Graphene-polymer composites: Implications for thermal management. *Heat Mass Transf.* **2020**, *56*, 1931–1945. [CrossRef]
79. Bhanuprakash, L.; Ali, A.; Mokkoth, R.; Varghese, S. Mode I and Mode II interlaminar fracture behavior of E-glass fiber reinforced epoxy composites modified with reduced exfoliated graphite oxide. *Polym. Compos.* **2018**, *39*, E2506–E2518. [CrossRef]
80. Ren, D.; Chen, L.; Yuan, Y.; Li, K.; Xu, M.; Liu, X. Designing and preparation of fiber-reinforced composites with enhanced interface adhesion. *Polymers* **2018**, *10*, 1128. [CrossRef]
81. Tang, L.; He, M.; Na, X.; Guan, X.; Zhang, R.; Zhang, J.; Gu, J. Functionalized glass fibers cloth/spherical BN fillers/epoxy laminated composites with excellent thermal conductivities and electrical insulation properties. *Compos. Commun.* **2019**, *16*, 5–10. [CrossRef]
82. Sundararajan, S.; Samui, A.B.; Kulkarni, P.S. Shape-stabilized poly(ethylene glycol) (PEG)-cellulose acetate blend preparation with superior PEG loading via microwave-assisted blending. *Sol. Energy* **2017**, *144*, 32–39. [CrossRef]
83. Nejman, A.; Cieślak, M.; Gajdzicki, B.; Goetzendorf-Grabowska, B.; Karaszewska, A. Methods of PCM microcapsules application and the thermal properties of modified knitted fabric. *Thermochim. Acta* **2014**, *589*, 158–163. [CrossRef]

84. Yang, G.; Wang, B.; Cheng, H.; Mao, Z.; Xu, H.; Zhong, Y.; Feng, X.; Yu, J.; Sui, X. Cellulosic scaffolds doped with boron nitride nanosheets for shape-stabilized phase change composites with enhanced thermal conductivity. *Int. J. Biol. Macromol.* **2020**, *148*, 627–634. [CrossRef]
85. You, J.; Choi, H.-H.; Lee, Y.M.; Cho, J.; Park, M.; Lee, S.-S.; Park, J.H. Plasma-assisted mechanochemistry to produce polyamide/boron nitride nanocomposites with high thermal conductivities and mechanical properties. *Compos. Part B Eng.* **2019**, *164*, 710–719. [CrossRef]
86. Khonsari, M.M.; Booser, E.R. *Applied Tribology: Bearing Design and Lubrication*; John Wiley & Sons, Ltd.: Hoboken, NJ, USA, 2017. [CrossRef]
87. Gwidon, W. *Stachowiak, Wear–Materials, Mechanisms and Practice*; John Wiley & Sons, Ltd.: Hoboken, NJ, USA, 2005. [CrossRef]
88. Wen, S.; Huang, P. *Principles of Tribology*; John Wiley & Sons Singapore Pte. Ltd.: Singapore, 2018. [CrossRef]
89. Bhushan, B.; Ko, P.L. Introduction to Tribology. *Appl. Mech. Rev.* **2003**, *56*, B6–B7. [CrossRef]
90. Finkin, E.F. Speculations on the theory of adhesive wear. *Wear* **1972**, *21*, 103–114. [CrossRef]
91. Abdellah, M.; Fathi, H.; Abdelhaleem, A.; Dewidar, M. Mechanical Properties and Wear Behavior of a Novel Composite of Acrylonitrile–Butadiene–Styrene Strengthened by Short Basalt Fiber. *J. Compos. Sci.* **2018**, *2*, 34. [CrossRef]
92. Janbesarayi, S.M.M.; Mohebi, M.; Baghshahi, S.; Alem, S.A.A.; Irom, E. Preparation of a Mesoporous Ceramic Adsorbent Based on Iranian Domestic Kaolin to Utilize as Slow-Release Urea Fertilizer Medium. *Iran. J. Mater. Sci. Eng.* **2020**, *17*, 30–38. [CrossRef]
93. Yusoff, Z.; Jamaludin, S.B. Tribology and development of wear theory. *Int. J. Curr. Res. Rev.* **2011**, *3*, 13–26.
94. Gunputh, U.F.; Le, H. A Review of In-Situ Grown Nanocomposite Coatings for Titanium Alloy Implant. *J. Compos. Sci.* **2020**, *4*, 41. [CrossRef]
95. Kraiklang, R.; Onwong, J.; Santhaweesuk, C. Multi-Performance Characteristics of AA5052 + 10% SiC Surface Composite by Friction Stir Processing. *J. Compos. Sci.* **2020**, *4*, 36. [CrossRef]
96. Hu, H.; Liu, Z.; Wang, C.; Meng, L.; Shen, Y. Nanomechanical Properties of a Bicomponent Epoxy Resin via Blending with Polyaryletherketone. *J. Compos. Sci.* **2019**, *3*, 92. [CrossRef]
97. Ferreira, F.; Pinheiro, I.; de Souza, S.; Mei, L.; Lona, L. Polymer Composites Reinforced with Natural Fibers and Nanocellulose in the Automotive Industry: A Short Review. *J. Compos. Sci.* **2019**, *3*, 51. [CrossRef]
98. Liu, Q.; Castillo-Rodríguez, M.; Galisteo, A.; de Villoria, R.G.; Torralba, J. Wear Behavior of Copper–Graphite Composites Processed by Field-Assisted Hot Pressing. *J. Compos. Sci.* **2019**, *3*, 29. [CrossRef]
99. Chhetri, S.; Samanta, P.; Murmu, N.; Kuila, T. Anticorrosion Properties of Epoxy Composite Coating Reinforced by Molybdate-Intercalated Functionalized Layered Double Hydroxide. *J. Compos. Sci.* **2019**, *3*, 11. [CrossRef]
100. Chhetri, S.; Adak, N.; Samanta, P.; Murmu, N.; Kuila, T. Exploration of Mechanical and Thermal Properties of CTAB-Modified MoS2/LLDPE Composites Prepared by Melt Mixing. *J. Compos. Sci.* **2018**, *2*, 37. [CrossRef]
101. Joseph, J.; Sharma, A.; Sahoo, B.; Paul, J.; Sidpara, A.M. PVA/MLG/MWCNT hybrid composites for X band EMI shielding—Study of mechanical, electrical, thermal and tribological properties. *Mater. Today Commun.* **2020**, *23*, 100941. [CrossRef]
102. Chen, P.; Zhang, Y.; Zhang, Z.; Li, R.; Zeng, S. Tuning the microstructure, mechanical properties, and tribological behavior of in-situ VCp-reinforced Fe—Matrix composites via manganese-partitioning treatment. *Mater. Today Commun.* **2020**, *24*, 101135. [CrossRef]
103. Cao, X.; Wang, J.; Liang, Y.; Zhang, G.; Shang, L.; Lu, Z.; Xue, Q. Corrosion and tribological investigations of the B4C coatings rubbing against SiC ball for high relative humidity engineering application. *Mater. Today Commun.* **2020**, *23*, 100924. [CrossRef]
104. Hou, W.; Gao, Y.; Wang, J.; Blackwood, D.J. Recent advances and future perspectives for graphene oxide reinforced epoxy resins. *Mater. Today Commun.* **2020**, *23*, 100883. [CrossRef]
105. Otsuki, M.; Matsukawa, H. Systematic Breakdown of Amontons' Law of Friction for an Elastic Object Locally. *Sci. Rep.* **2013**, *3*, 1586. [CrossRef] [PubMed]
106. Alem, S.A.A.; Latifi, R.; Angizi, S.; Mohamadbeigi, N.; Rajabi, M.; Ghasali, E.; Orooji, Y. Development of Metal Matrix Composites and Nanocomposites Via Double-Pressing Double-Sintering (DPDS) Method. *Mater. Today Commun.* **2020**, *25*, 101245. [CrossRef]

107. Alem, S.A.A.; Latifi, R.; Angizi, S.; Hassanaghaei, F.; Aghaahmadi, M.; Ghasali, E.; Rajabi, M. Microwave sintering of ceramic reinforced metal matrix composites and their properties: A review. *Mater. Manuf. Process.* **2020**, *35*, 303–327. [CrossRef]
108. Kumar, M.S.; Mangalaraja, R.V.; Kumar, R.S.; Natrayan, L. Processing and Characterization of AA2024/Al2O3/SiC Reinforces Hybrid Composites Using Squeeze Casting Technique. *Iran. J. Mater. Sci. Eng.* **2019**, *16*, 55–67. [CrossRef]
109. Akbarzadeh, M.; Zandrahimi, M.; Moradpour, E. Effect of Substrate Bias Voltage and Ti Doping on the Tribological Properties of DC Magnetron Sputtered MoSx Coatings. *Iran. J. Mater. Sci. Eng.* **2019**, *16*, 10–20. [CrossRef]
110. Jeyaprakash, N.; Yang, C. Comparative study of NiCrFeMoNb / FeCrMoVC laser cladding process on nickel-based superalloy ABSTRACT. *Mater. Manuf. Process.* 2020. [CrossRef]
111. Sarmah, A.; Kar, S.; Patowari, P.K.; Sarmah, A. Surface modification of aluminum with green compact powder metallurgy Inconel-aluminum tool in EDM. *Mater. Manuf. Process.* **2020**. [CrossRef]
112. Tyagi, R.; Pandey, K.; Das, A.K.; Mandal, A. Deposition of hBN + Cu layer through electrical discharge process using green compact electrode. *Mater. Manuf. Process.* **2019**. [CrossRef]
113. Jeyaprakash, N.; Yang, C.; Sivasankaran, S. Laser cladding process of Cobalt and Nickel based hard-micron-layers on 316L-stainless-steel-substrate. *Mater. Manuf. Process.* **2019**, *35*, 142–151. [CrossRef]
114. Khajehzadeh, M.; Moradpour, J.; Razfar, M.R. Influence of nanolubricant particles ' size on flank wear in hard turning. *Mater. Manuf. Process.* **2019**, *34*, 494–501. [CrossRef]
115. Shoushtari, M.T.; Goodarzi, M.; Sabet, H. Investigation of Microstructure and Dry Sliding Wear of Hardfaced Layers Produced by FCAW Using Cored Wire Fe-B-C-Ti Alloy, Iran. *J. Mater. Sci. Eng.* **2019**, *15*, 19–32. [CrossRef]
116. Yan, Y. Tribology and Tribo-Corrosion Testing and Analysis of Metallic Biomaterials. In *Met. Biomed. Devices*; Woodhead Publishing Series in Biomaterials; Elsevier: Amsterdam, The Netherlands, 2010; pp. 178–201. [CrossRef]
117. Maru, M.M.; Tanaka, D.K. Consideration of Stribeck Diagram Parameters in the Investigation on Wear and Friction Behavior in Lubricated Sliding. *J. Braz. Soc. Mech. Sci. Eng.* **2007**, *29*, 55–62. [CrossRef]
118. Robinson, J.W.; Zhou, Y.; Bhattacharya, P.; Erck, R.; Qu, J.; Timothy, J. Probing the molecular design of hyper-branched aryl polyesters towards lubricant applications. *Sci. Rep.* **2016**, *6*, 18624. [CrossRef]
119. Uflyand, I.E.; Zhinzhilo, V.A.; Burlakova, V.E. Metal-containing nanomaterials as lubricant additives: State-of-the-art and future development. *Friction* **2019**, *7*, 93–116. [CrossRef]
120. Wang, H.; Xu, B.; Liu, J.; Wang, H.; Xu, B.; Liu, J. Solid Lubrication Materials. In *Micro Nano Sulfide Solid Lubr*; Springer: Berlin/Heidelberg, Germany, 2012; pp. 1–10. [CrossRef]
121. Busch, C. Solid Lubrication. In *Lubr*; Lubr., WILEY-VCH Verlag GmbH & Co. KGaA: Weinheim, Germany, 2017; pp. 843–880. [CrossRef]
122. Prajapati, A.K.; Omrani, E.; Menezes, P.L.; Rohatgi, P.K. Fundamentals of Solid Lubricants. In *Self-Lubricating Compos*; Springer-Verlag: Berlin, Germany, 2018; pp. 1–32. [CrossRef]
123. Kumar, P.; Mallick, A.; Kujur, M.S.; Tun, K.S.; Gupta, M. Synthesis and analysis of Mg–3% Al alloy nanocomposites reinforced by RGO. *Mater. Manuf. Process.* **2020**. [CrossRef]
124. Ferreira, R.; Martins, J.; Carvalho, Ó.; Sobral, L.; Carvalho, S.; Silva, F. Tribological solutions for engine piston ring surfaces: An overview on the materials and manufacturing. *Mater. Manuf. Process.* **2020**, *35*, 498–520. [CrossRef]
125. Bajakke, P.A.; Malik, V.R.; Deshpande, A.S. Particulate metal matrix composites and their fabrication via friction stir processing–a review. *Mater. Manuf. Process.* **2019**, *34*, 833–881. [CrossRef]
126. Litwin, W.; Dymarski, C. Experimental research on water-lubricated marine stern tube bearings in conditions of improper lubrication and cooling causing rapid bush wear. *Tribol. Int.* **2016**, *95*, 449–455. [CrossRef]
127. Golchin, A.; Friedrich, K.; Noll, A.; Prakash, B. Influence of counter surface topography on the tribological behavior of carbon-filled PPS composites in water. *Tribol. Int.* **2015**, *88*, 209–217. [CrossRef]
128. Gao, C.P.; Guo, G.F.; Zhao, F.Y.; Wang, T.M.; Jim, B.; Wetzel, B.; Zhang, G.; Wang, Q.H. Tribological behaviors of epoxy composites under water lubrication conditions. *Tribol. Int.* **2016**, *95*, 333–341. [CrossRef]
129. Giasson, S.; Lagleize, J.M.; Rodríguez-Hernández, J.; Drummond, C. Boundary lubricant polymer films: Effect of cross-linking. *Langmuir* **2013**, *29*, 12936–12949. [CrossRef]

130. Xie, G.Y.; Sui, G.X.; Yang, R. Effects of potassium titanate whiskers and carbon fibers on the wear behavior of polyetheretherketone composite under water lubricated condition. *Compos. Sci. Technol.* **2011**, *71*, 828–835. [CrossRef]
131. Cho, D.; Kim, J.; Kwon, S.; Lee, C.; Lee, Y. Evaluation of hexagonal boron nitride nano-sheets as a lubricant additive in water. *Wear* **2013**, *302*, 981–986. [CrossRef]
132. Martin, J.M.; Mogne, T.L.; Chassagnette, C.; Gardos, M.N. Friction of Hexagonal Boron Nitride in Various Environments. *Tribol. Trans.* **1992**, *35*, 462–472. [CrossRef]
133. Saito, T.; Honda, F. Chemical contribution to friction behavior of sintered hexagonal boron nitride in water. *Wear* **2000**, *237*, 253–260. [CrossRef]
134. Saito, T.; Imada, Y.; Honda, F. Chemical influence on wear of Si3N4 and hBN in water. *Wear* **1999**, *236*, 153–158. [CrossRef]
135. Cao, Y.; Du, L.; Huang, C.; Liu, W.; Zhang, W. Applied Surface Science Wear behavior of sintered hexagonal boron nitride under atmosphere and water vapor ambiences. *Appl. Surf. Sci.* **2011**, *257*, 10195–10200. [CrossRef]
136. Erdemir, A.; Fenske, G.R.; Erck, R.A. A study of the formation and self-lubrication mechanisms of boric acid films on boric oxide coatings. *Surf. Coatings Technol.* **1990**, *43–44*, 588–596. [CrossRef]
137. Gao, C.; Guo, G.; Zhang, G.; Wang, Q.; Wang, H. Formation mechanisms and functionality of boundary films derived from water lubricated polyoxymethylene/hexagonal boron nitride nanocomposites. *Mater. Des.* **2017**, *115*, 276–286. [CrossRef]
138. Garton, A.; Mclean, P.D.; Wiebe, W.; Densley, R.J. Exposure of Cross-linked Epoxy Resins to the Space Environment. *J. Appl. Polym. Sci.* **1986**, *32*, 3941–3957. [CrossRef]
139. Chang, L.; Zhang, Z.; Ye, L.; Friedrich, K. Tribological properties of epoxy nanocomposites III. Characteristics of transfer films. *Wear* **2007**, *262*, 699–706. [CrossRef]
140. Yu, J.; Zhao, W.; Wu, Y.; Wang, D.; Feng, R. Tribological properties of epoxy composite coatings reinforced with functionalized C-BN and H-BN nanofillers. *Appl. Surf. Sci.* **2018**, *434*, 1311–1320. [CrossRef]
141. Zhao, W.; Zhao, W.; Huang, Z.; Liu, G.; Wu, B. Tribological performances of epoxy resin composite coatings using hexagonal boron nitride and cubic boron nitride nanoparticles as additives. *Chem. Phys. Lett.* **2019**, *732*, 136646. [CrossRef]
142. Panda, J.N.; Bijwe, J.; Pandey, R.K. Optimization of the amount of short glass fibers for superior wear performance of PAEK Composites. *Compos. Part A* **2019**, *116*, 158–168. [CrossRef]
143. Panda, J.N.; Bijwe, J.; Pandey, R.K. Role of micro and nano-particles of hBN as a secondary solid lubricant for improving tribo-potential of PAEK composite. *Tribol. Int.* **2019**, *130*, 400–412. [CrossRef]
144. Mainzer, B.; Lin, C.; Jemmali, R.; Frieß, M.; Riedel, R.; Koch, D. Characterization and application of a novel low viscosity polysilazane for the manufacture of C- and SiC-fiber reinforced SiCN ceramic matrix composites by PIP process. *J. Eur. Ceram. Soc.* **2019**, *39*, 212–221. [CrossRef]
145. Zhou, W.; Long, L.; Xiao, P.; Jia, C.; Li, Y. Comparison in dielectric and microwave absorption properties of SiC coated carbon fi bers with PyC and BN interphases. *Surf. Coat. Technol.* **2019**, *359*, 272–277. [CrossRef]
146. Nötha, A.; Maier, J.; Schönfeld, K.; Klemm, H. Wet chemical deposition of BN, SiC and Si3N4 interphases on SiC fibers. *J. Eur. Ceram. Soc.* **2020**. [CrossRef]
147. Tak, W.S.; Uk, J.; Young, H.; Jeong, K.; Sik, W. Coating with boron nitride on SiC fiber using atomic substitution. *J. Korean Ceram. Soc.* **2020**, *57*, 200–205. [CrossRef]
148. Kuang, W.; Zhao, B.; Yang, C.; Ding, W. Effects of h-BN particles on the microstructure and tribological property of self-lubrication CBN abrasive composites. *Ceram. Int.* **2020**, *46*, 2457–2464. [CrossRef]
149. Chen, W.; Zhang, D.; Lv, Z.; Li, H. Self-lubricating mechanisms via the in situ formed tribo-film of sintered ceramics with hBN addition in a high humidity environment. *Int. J. Refract. Metals Hard Mater.* **2017**, *66*, 163–173. [CrossRef]
150. Chen, W.; Wang, K.; Liu, X.; He, N.; Xin, H.; Hao, W. Investigation of the friction and wear characteristics of Si3N4-hBN ceramic composites under marine atmospheric environment. *Int. J. Refract Met. Hard Mater.* **2019**, *81*, 345–357. [CrossRef]
151. Yuan, J.; Zhang, Z.; Yang, M.; Wu, L.; Li, P.; Guo, F.; Men, X.; Liu, W. Coupling hybrid of BN nanosheets and carbon nanotubes to enhance the mechanical and tribological properties of fabric composites. *Compos. Part A Appl. Sci. Manuf.* **2019**, *123*, 132–140. [CrossRef]

152. Liu, F.; Ji, Y.; Sun, Z.; Wang, G.; Bai, Y. Enhancing corrosion resistance of Al-Cu/AZ31 composites synthesized by a laser cladding and FSP hybrid method. *Mater. Manuf. Process.* **2019**, *34*, 1458–1466. [CrossRef]
153. Dodla, S. Micromechanical Analysis for Two-Phase Copper-Silver Composites under Large Deformations. *J. Compos. Sci.* **2017**, *2*, 1. [CrossRef]
154. Fathy, A.; Shehata, F.; Abdelhameed, M.; Elmahdy, M. Compressive and wear resistance of nanometric alumina reinforced copper matrix composites. *Mater. Des.* **2012**, *36*, 100–107. [CrossRef]
155. Elkady, O.A.M.; Abu-Oqail, A.; Ewais, E.M.M.; El-Sheikh, M. Physico-mechanical and tribological properties of Cu/h-BN nanocomposites synthesized by PM route. *J. Alloy. Compd.* **2015**, *625*, 309–317. [CrossRef]
156. Palanivel, R.; Dinaharan, I.; Laubscher, R.F.; Davim, J.P. Influence of boron nitride nanoparticles on microstructure and wear behavior of AA6082/TiB2 hybrid aluminum composites synthesized by friction stir processin. *Mater. Des.* **2016**, *106*, 195–204. [CrossRef]
157. Chi, H.; Jiang, L.; Chen, G.; Kang, P.; Lin, X.; Wu, G. Dry sliding friction and wear behavior of (TiB_2 + h − BN)/2024Al composites. *Mater. Des.* **2015**, *87*, 960–968. [CrossRef]
158. Rajan, H.B.M.; Ramabalan, S.; Dinaharan, I.; Vijay, S.J. Effect of TiB2 content and temperature on sliding wear behavior of AA7075/TiB2 in situ aluminum cast composites. *Arch. Civ. Mech. Eng.* **2014**, *14*, 72–79. [CrossRef]
159. Song, Y.; He, G.; Wang, Y.; Chen, Y. Tribological behavior of boron nitride nanoplatelet reinforced Ni_3 Al intermetallic matrix composite fabricated by selective laser melting. *Mater. Des.* **2019**, *165*, 107579. [CrossRef]
160. Zhang, Z.; Chen, D.L. Consideration of Orowan strengthening effect in particulate-reinforced metal matrix nanocomposites: A model for predicting their yield strength. *Scr. Mater.* **2006**, *54*, 1321–1326. [CrossRef]
161. Gautam, R.K.S.; Rao, U.S.; Tyagi, R. High temperature tribological properties of Ni-based self-lubricating coatings deposited by atmospheric plasma spray. *Surf. Coat. Technol.* **2019**, *372*, 390–398. [CrossRef]
162. Li, B.; Jia, J.; Gao, Y.; Han, M.; Wang, W. Microstructural and tribological characterization of NiAl matrix self-lubricating composite coatings by atmospheric plasma spraying. *Tribol. Int.* **2017**, *109*, 563–570. [CrossRef]
163. Hammes, G.; Mucelin, K.J.; da Costa Gonçalves, P.; Binder, C.; Binder, R.; Janssen, R.; Klein, A.N.; de Mello, J.D.B. Effect of hexagonal boron nitride and graphite on mechanical and scuffing resistance of self lubricating iron based composite. *Wear* **2017**, *376–377*, 1084–1090. [CrossRef]
164. Kadiyala, A.K.; Bijwe, J. Surface lubrication of graphite fabric reinforced epoxy composites with nano- and micro-sized hexagonal boron nitride. *Wear* **2013**, *301*, 802–809. [CrossRef]
165. De Mello, J.D.B.; Binder, C.; Binder, R.; Klein, A.N. Effect of precursor content and sintering temperature on the scuffing resistance of sintered self lubricating steel. *Wear* **2011**, *271*, 1862–1867. [CrossRef]
166. Kimura, Y.; Wakabayashi, T.; Okada, K.; Wada, T.; Nishikaw, H. Boron nitride as a lubricant additive. *Wear* **1999**, *232*, 199–206. [CrossRef]
167. Abdullah, M.I.H.C.; Abdollah, M.F.B.; Tamaldin, N.; Amiruddin, H.; Nuri, N.R.M. Effect of hexagonal boron nitride nanoparticles as an additive on the extreme pressure properties of engine oil. *Ind. Lubr. Tribol.* **2016**, *68*, 441–445. [CrossRef]
168. Wan, Q.; Jin, Y.; Sun, P.; Ding, Y. Tribological behaviour of a lubricant oil containing boron nitride nanoparticles. *Procedia Eng.* **2015**, *102*, 1038–1045. [CrossRef]
169. Songfeng, E.; Ye, X.; Zhu, Z.; Lu, W.; Li, C. Tuning the structures of boron nitride nanosheets by template synthesis and their application as lubrication additives in water. *Appl. Surf. Sci.* **2019**, *479*, 119–127. [CrossRef]
170. Liu, Y.; Mateti, S.; Li, C.; Liu, X.; Glushenkov, A.M.; Liu, D.; Li, H.; Fabijanic, D.; Chen, Y.I.; Chen, P.Y.I. Synthesis of Composite Nanosheets of Graphene and Boron Nitride and Their Lubrication Application in Oil. *Adv. Eng. Mater.* **2018**, *20*, 1700488. [CrossRef]
171. Ci, X.; Zhao, W.; Luo, J. A sustainable interlayer slip leads to the excellent tribological behaviour of hexagonal boron nitride microsheets. *Colloids Surf. A Physicochem. Eng. Asp.* **2020**, *598*, 124859. [CrossRef]
172. Hu, Y.; Wang, Y.; Zeng, Z.; Zhao, H.; Ge, X.; Wang, K.; Wang, L.; Xue, Q.; Hu, Y.; Wang, Y.; et al. PEGlated Graphene as Nanoadditive for Enhancing the Tribological Properties of Water-based. *Carbon N. Y.* **2018**, *137*, 41–48. [CrossRef]
173. Kumari, S.; Sharma, O.P.; Gusain, R.; Mungse, H.P.; Kukrety, A.; Kumar, N.; Sugimura, H.; Khatri, O.P. Alkyl-Chain-Grafted Hexagonal Boron Nitride Nanoplatelets as Oil-Dispersible Additives for Friction and Wear Reduction. *ACS Appl. Mater. Interfaces* **2015**, *7*, 3708–3716. [CrossRef]

174. Suresha, B.; Shenoy, R.S.; Bhat, R.; Sohan, P.K.; Hemanth, R. Optimization of wear behaviour of boron nitride filled polyaryletherketone composites by Taguchi approach. *Mater. Res. Express.* **2019**, *6*. [CrossRef]
175. Navaneethakrishnan, G.; Karthikeyan, T.; Saravanan, S.; Selvam, V. Influence of boron nitride on morphological, mechanical, thermal and wear characteristics of epoxy nanocomposites. *Mater. Res. Innov.* **2019**, *24*, 1–6. [CrossRef]
176. Li, X.; Gao, Y.; Wei, S.; Yang, Q. Crossmark. *Ceram. Int.* **2017**, *43*, 1578–1583. [CrossRef]
177. Chen, W.; Wang, Z.; Gao, Y.; Li, H.; He, N. Microstructure, mechanical properties and friction/ wear behavior of hot-pressed Si3N4/BN ceramic composites. *Ceram. Silik.* **2019**, *63*, 1–10. [CrossRef]
178. Zhao, Y.; Feng, K.; Yao, C.; Nie, P.; Huang, J.; Li, Z. Microstructure and tribological properties of laser cladded self-lubricating nickel-base composite coatings containing nano-Cu and h-BN solid lubricants. *Surf. Coat. Technol.* **2019**, *359*, 485–494. [CrossRef]
179. Gopinath, S.; Prince, M.; Raghav, G.R. Enhancing the mechanical, wear and corrosion behaviour of stir casted aluminium 6061 hybrid composites through the incorporation of boron nitride and aluminium oxide particles. *Mater. Res. Express.* **2020**, *7*. [CrossRef]
180. Chen, Z.; Yan, H.; Zhang, P.; Yu, Z.; Lu, Q.; Guo, J. Microstructural evolution and wear behaviors of laser-clad Stellite 6/NbC/h-BN self-lubricating coatings. *Surf. Coatings Technol.* **2019**, *372*, 218–228. [CrossRef]